Introduction to CMS Physics and Detector (PhD level)

(Extracted from 2003 PhD thesis of Nicola Amapane).

Università degli Studi di Torino

Facoltà di Scienze Matematiche, Fisiche e Naturali
Dottorato di Ricerca in Fisica - XV ciclo

Development and Performance of High Level Trigger Algorithms for the Muon Trigger of the CMS Experiment

Tutore
Prof.sa Alessandra Romero

Coordinatore
Prof. Ezio Menichetti

Candidato
Dott. Nicola Amapane

24 Gennaio 2003

Chapter 1

Physics with the Large Hadron Collider

The Large Hadron Collider (LHC) is a proton-proton collider under construction at CERN. With a centre-of-mass energy of 14 TeV and a design luminosity of $10^{34}\text{cm}^{-2}\text{s}^{-1}$, it is a machine of unprecedented complexity and potential.

This chapter introduces the motivation, the design and the physics programme of LHC. In Section 1.1, a short overview of the Standard Model is given, with the aim of introducing the open issues that LHC is expected to explore. The design of the LHC, the experimental environment and the requirements for LHC experiments are described in Section 1.2. Finally, an overview of the main physics studies feasible at the LHC is presented in Section 1.3.

1.1 The Standard Model

The Standard Model (SM) of fundamental interactions describes matter as composed by half-integer spin particles, the *fermions*, that can be divided in two main groups: *leptons*, including electrons, muons, taus and neutrinos, and *quarks*. The latter have fractional charge and do not freely exist in nature; they are the constituents of a wide class of particles, the *hadrons*. Examples of hadrons are protons and neutrons, which are both composed by three quarks. A classification of fermions is given in Table 1.1.

Interactions between particles are described in terms of the exchange of *bosons*, integer spin particles that mediate fundamental interactions. *Gravitation* is the interaction closest to common experience; however it is not relevant at the scales of mass and distance typical of particle physics. The bond between atoms and molecules is due to the *electromagnetic interaction*, while the *weak interaction* explains, for example, nuclear β-decays. Finally, the *strong interaction* is responsible for the confinement of quarks inside hadrons. The

Table 1.1: *Classification of the three families of fundamental fermions.*

Fermions	1^{st} fam.	2^{nd} fam.	3^{rd} fam.	Charge	Interactions
Quarks	u	c	t	$+\frac{2}{3}$	All
	d	s	b	$-\frac{1}{3}$	
Leptons	e	μ	τ	-1	Weak, E.M.
	ν_e	ν_μ	ν_τ	0	Weak

characteristics of electromagnetic, weak and strong interactions are summarised in Table 1.2.

Table 1.2: *Fundamental interactions relevant in particle physics.*

	Electromagnetic	Weak	Strong
Quantum	Photon (γ)	$W^{\pm}$ and Z	Gluons
Mass (GeV/c^2)	0	80–90	0
Coupling constant	$\alpha(Q^2 = 0) \approx \frac{1}{137}$	$G_F \approx 1.2 \times 10^{-5}\,\mathrm{GeV}^{-2}$	$\alpha_s(m_\mathrm{Z}) \approx 0.1$
Range (cm)	∞	10^{-16}	10^{-13}

The Standard Model describes these interactions with two gauge theories:

- the theory of the electroweak interaction, or Electroweak Standard Model, that unifies the electromagnetic and weak interactions;
- the theory of strong interactions or Quantum Chromodynamics (QCD).

A comprehensive description of the Electroweak Standard Model is outside the scope of this work. However, the main results are reviewed in the following section.

1.1.1 Electroweak Symmetry Breaking in the Standard Model

The theory of electromagnetic interactions is called Quantum Electrodynamics (QED), and is based on the invariance of the Lagrangian for local gauge transformations with respect to the U(1) symmetry group. This condition leads to the existence of a massless vector field, the photon.

The unification of the theory of electromagnetism and that of weak interactions is accomplished by extending the symmetry to the group SU(2)×U(1) [5], which is associated to the quantum numbers I (*weak isospin*) and Y (*hypercharge*), that satisfy the relation:

$$Q = I_3 + \frac{Y}{2}, \tag{1.1}$$

where I_3 is the third component of the weak isospin and Q is the electric charge.

The invariance for local gauge transformations with respect to the SU(2)×U(1) group introduces four massless vector fields, $W_\mu^{1,2,3}$ and B_μ, that couple to fermions with two coupling constants, g and g'. The corresponding physical fields are linear combinations of $W_\mu^{1,2,3}$ and B_μ: the charged bosons W^+ and W^- correspond to

$$\mathrm{W}_\mu^\pm = \sqrt{\frac{1}{2}}(\mathrm{W}_\mu^1 \pm i\mathrm{W}_\mu^2), \tag{1.2}$$

while the neutral bosons γ and Z correspond to

$$A_\mu = B_\mu \cos\theta_W + W_\mu^3 \sin\theta_W \tag{1.3}$$
$$Z_\mu = -B_\mu \sin\theta_W + W_\mu^3 \cos\theta_W, \tag{1.4}$$

obtained by mixing the neutral fields W_μ^3 and B_μ with a rotation defined by the *Weinberg angle* θ_W. The field A_μ is then identified with the tensor of the electromagnetic field; requiring the coupling terms to be equal, one obtains

$$g \sin\theta_W = g' \cos\theta_W = e \tag{1.5}$$

that represents the electroweak unification.

Up to this point, all particles are massless: in the SU(2)×U(1) Lagrangian a mass term for the gauge bosons would violate gauge invariance. Masses are introduced with the *Higgs mechanism*, that allows fermions and the $W^\pm$ and Z bosons to be massive, while keeping the photon massless. This is accomplished by introducing the Higgs field, a SU(2) doublet of complex scalar fields:

$$\phi = \begin{pmatrix} \phi^+ \\ \phi^0 \end{pmatrix} = \frac{1}{\sqrt{2}} \begin{pmatrix} \phi_1 + i\phi_2 \\ \phi_3 + i\phi_4 \end{pmatrix}. \tag{1.6}$$

The Lagrangian of this field must be invariant under SU(2)×U(1) local gauge transformations, and includes a potential term

$$V(\phi) = -\mu^2 \phi^\dagger \phi + \lambda(\phi^\dagger \phi)^2, \tag{1.7}$$

where $\mu^2 > 0$ and $\lambda > 0$, so that the potential has a minimum for

$$\phi^\dagger\phi = \frac{1}{2}(\phi_1^2 + \phi_2^2 + \phi_3^2 + \phi_4^2) = \frac{\mu^2}{2\lambda} \equiv \frac{v^2}{2}. \tag{1.8}$$

One is free to choose the values of $\phi_i = 0$ that respect this condition; the fact that the minimum is not found for $\phi_i = 0$, but for a manifold of values, is called *spontaneous symmetry breaking*.

Boson masses derive from the coupling of the boson fields with the non-zero vacuum value of the Higgs field: the potential in its fundamental state does not have the symmetry properties of the Lagrangian. However, it can be shown that the minimum for the Higgs field is invariant for U(1) transformations; the electromagnetic U(1) symmetry is unbroken and the photon remains massless.

The Higgs mechanism gives rise to three massive gauge bosons, corresponding to nine degrees of freedom. Since the initial number of independent fields is ten (three massless bosons with two polarisations states each, plus the four real ϕ_i fields), one additional scalar gauge boson should appear as a real particle. This is the Higgs boson. Its mass depends on v and λ; the value of v is related to the boson masses by the relations:

$$m_{W^\pm} = \frac{1}{2}gv; \qquad m_Z = \frac{gv}{2\cos\theta_W} \tag{1.9}$$

However the parameter λ is characteristic of the field ϕ and cannot be determined from other measurements, so the Higgs mass is unknown.

The fermion masses are generated with a similar mechanism, but appear as free parameters of the theory, six for the quarks and three for the leptons (assuming neutrinos to be massless). These bring the number of free parameters of the Standard model to 17, the others being the four independent elements of the Cabibbo-Kobayashi-Maskawa matrix that describes the mixing of quark flavours, the couplings g and g', the parameter v of the Higgs vacuum expectation value and the Higgs mass.

All these parameters, except the mass of the Higgs boson which has not yet been observed, can be determined from experimental quantities. The measurement of these quantities allows therefore a consistency check of the electroweak Standard Model, which up to now has been confirmed with very high accuracy.

1.1.2 Higgs Mass

The mass m_H of the Higgs boson is not predicted by the SM; however constraints on its value can be obtained from theoretical considerations.

First of all, the Higgs potential of Eq. (1.7) is affected by radiative corrections, which involve the mass of bosons and fermions and depend on the

renormalisation scale Λ. Radiative corrections might change the shape of the potential so that it has no more an absolute minimum; vacuum would then become unstable. The request of *vacuum stability*, *i.e.* that the λ coefficient is large enough to avoid instability up to a certain scale Λ, implies a lower bound on the Higgs mass. On the other hand, due to the running of the coupling, λ increases with the energy scale; the request that it remains finite up to a scale Λ (*triviality*) corresponds to an upper bound on m_H.

In both cases, the parameter Λ represents the scale up to which the Standard Model is taken to be valid. The theoretical bounds on m_H as a function of Λ are shown in Fig. 1.1.

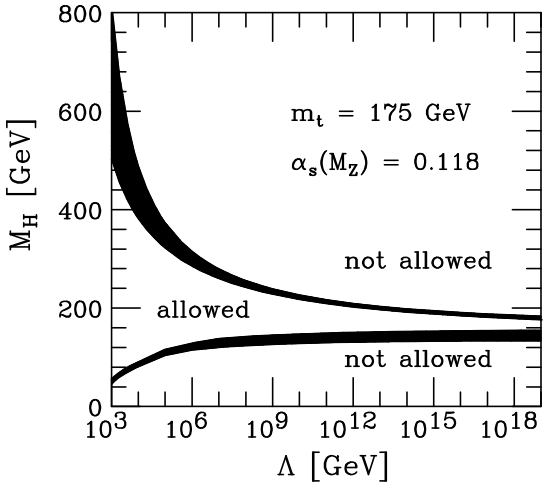

Figure 1.1: *Theoretical bounds on the Higgs mass as a function of the energy scale Λ up to which the Standard Model is valid [6].*

For the SM to remain valid up to the Planck scale ($\Lambda = 10^{19}$ GeV), the Higgs mass must be in the range 130-200 GeV/c^2. Assuming the SM to be valid only up to $\Lambda \sim 1$ TeV, the Higgs mass can be up to 700 GeV/c^2. In any case, new colliders should search for the Higgs boson up to masses of the order of ≈ 1 TeV. This is one of the guidelines for the design of the LHC. If the Higgs is not found in this range, then a more sophisticated explanation of the electroweak symmetry breaking mechanism must be found.

Experimental bounds on m_H are provided by measurements at LEP, SLC and Tevatron [7]. Direct searches excluded the region below 112.3 GeV/c^2 at 95% confidence level. Precision electroweak measurements are (logarithmically) sensitive to the Higgs mass due to radiative corrections; electroweak data can therefore be fitted taking m_H as free parameter. In Fig. 1.2, the shape of the χ^2 of the fit is shown as a function of m_H. The curve is shallow and the minimum is below the value excluded by direct searches (shaded area). One may conclude

nevertheless that the fit privileges low values of the Higgs mass. An upper limit of 170 GeV/c^2 can be set at 95% confidence level.

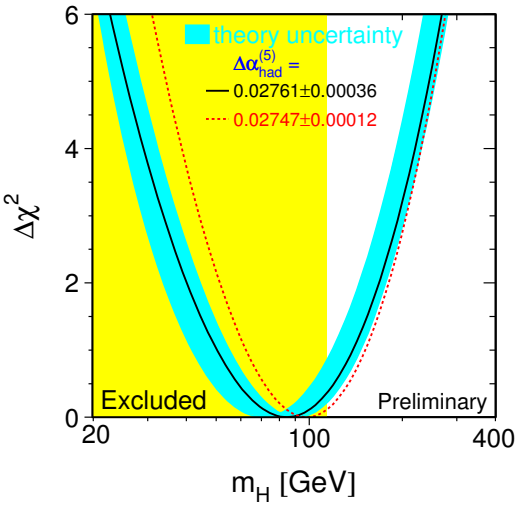

Figure 1.2: *$\Delta\chi^2$ of the fit of electroweak measurements of LEP, SLC and Tevatron as a function of the Higgs mass [7].*

1.1.3 Open Questions

Even if up to now the SM has been experimentally confirmed with very high accuracy, the Higgs boson has never been observed, and has been excluded by direct searches up to the energies accessible at LEP.

Apart from this problem, there are several reasons to think that the Standard Model is only an effective description, and that a more fundamental theory must exist. We already observed that theoretical bounds on the Higgs mass can be derived from the request that, once radiative corrections are included, the theory remains valid up to a given energy scale. It is natural to think that at higher energy scales some more general theory should be valid, possibly describing all interactions. In the Standard Model, the strong interaction is described by a SU(3) "colour" symmetry group, which however is not unified with the electroweak description. Gravity, whose strength should become comparable with that of other interactions at the Planck scale (10^{19} GeV), is not included at all. It would be appealing to find a wider symmetry that describes all interactions, and the reason why it is broken at these energy scales.

In addition, the Higgs mass suffers from divergences caused by radiative corrections which are proportional to the energy cutoff; for the Standard Model to be valid up to very high energy scales, extremely precise cancellations should be present at all perturbation levels. Such cancellations are formally possible, but there is no reason why such a fine tuning should occur (*naturalness problem*).

Other considerations of more aesthetic nature are that the Higgs is an ad-hoc addition to the Standard Model; moreover it is the only scalar particle in the theory. Also, there is no explanation for the fact that the particle masses would be significantly smaller than the energy scale up to which the theory remains valid (*hierarchy problem*). Finally, the number of free parameters of the Standard model (17, neglecting neutrino masses and mixings) appears too high not to be artificial.

Several solutions for these problems have been proposed. Among them, supersymmetry (SUSY) is an elegant theory that introduces a new symmetry between bosons and fermions. SUSY predicts that each particle has a supersymmetric partner whose spin differs by one half. The naturalness problem is solved by the fact that the loop contributions from particles and their supersymmetric partners cancel. The simplest supersymmetric model, called the Minimal Supersymmetric Standard Model (MSSM), requires at least two Higgs doublets, corresponding to five Higgs particles: two charged bosons, $H^{\pm}$, two scalar bosons, h and H, and one pseudo-scalar, A. The MSSM predicts a rich phenomenology to appear below energies of about 1 TeV; however no evidence for supersymmetry has been observed yet.

1.2 The Large Hadron Collider

1.2.1 Design of the LHC

From the discussion of the previous section we know that the main task of today's experimental particle physics is the search of the Higgs boson (or other phenomena) up to a scale of about 1 TeV. This section discusses the requirements and feasibility of a collider designed for this search, the LHC.

In a circular collider of radius R, the energy loss per turn due to synchrotron radiation is proportional to $E^4/(m^4 R)$, where E and m are respectively the energy and mass of the particles accelerated. Circular electron colliders would need enormous dimensions to reach energies of the order of 500 GeV per beam, so the natural choice for a collider with current technologies is to use beams of protons, which are almost 2000 times heavier than electrons. Protons are not elementary particles, and in hard collisions the interaction involves their constituents (quarks and gluons), which carry only a fraction of the proton energy. While this fact has the drawback that the centre-of-mass energy and

the rest frame of the hard scattering are unknown, it has the advantage that a wide range of energies can be explored with fixed-energy beams.

Since only a fraction of the proton energy is exchanged in the hard scattering, the centre-of-mass energy of the beams must be much higher than the mass of the particle that has to be produced. The cross section for different processes as a function of the centre-of-mass energies in $p-p$ collisions is shown in Fig. 1.3. It can be noted that the Higgs cross section increases steeply with the centre-

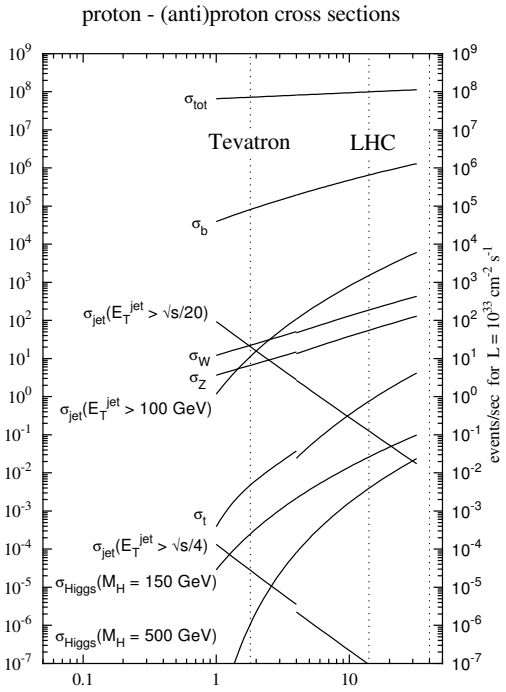

Figure 1.3: *Cross sections and event rates of several processes as a function of the centre-of-mass energy of proton-proton collisions [8].*

of-mass energy, while the total cross section (*i.e.* the background) remains almost constant. It is clear that the highest possible centre-of-mass energy should be used. The cross-section σ determines the event rate R of a given process according to the formula $R = \mathcal{L}\sigma$. The factor $\mathcal{L}$ is called *luminosity*; it represents the number of collisions per unit time and cross-sectional area of the beams. It is specific to the collider parameters and does not depend on the interaction considered:

$$\mathcal{L} = f\frac{n_1 n_2}{A}. \tag{1.10}$$

Here f is the collision frequency of bunches composed of n_1 and n_2 particles and A is the overlapping cross-sectional area of the beams.

With a centre-of-mass energy of 40 TeV, the Superconducting Super Collider (SSC), a $p-p$ collider to be constructed in the USA, would have been a perfect

Table 1.3: *LHC parameters for $p-p$ and Pb–Pb collisions.*

Parameter	$p-p$	$^{208}Pb^{82+}$
Centre-of-mass energy (TeV)	14	1148
Number of particles per bunch	1.1×10^{11}	$\sim 8\times10^{7}$
Number of bunches	2808	608
Design Luminosity ($cm^{-2}s^{-1}$)	10^{34}	2×10^{27}
Luminosity lifetime (h)	10	4.2
Bunch length (mm)	53	75
Beam radius at interaction point (μm)	15	15
Time between collisions (ns)	24.95	124.75×10^{3}
Bunch crossing rate (MHz)	40.08	0.008
Circumference (km)	26.659	
Dipole field (T)	8.3	8.3

candidate for the search of the Higgs. Unfortunately, this project was abandoned due to financial problems while its 87 km long tunnel was being excavated. The idea behind the Large Hadron Collider is to reuse the existing 27 km long LEP tunnel to install a new proton collider. Considerable financial savings are obtained from the fact that the tunnel and several infrastructures (including pre-accelerators) already exist. However, the size of the tunnel limits the centre-of-mass energy to 14 TeV, since the beams must be bent by dipole magnets whose maximum field is limited.

To compensate for the lower Higgs production cross sections, the LHC must have a very high luminosity; this has the drawback that the total event rate becomes so high that several interactions overlap in the same bunch crossing (*pile up*). The LHC will operate at a bunch crossing rate of 40 MHz and a design LHC luminosity of $10^{34}cm^{-2}s^{-1} = 10\ nb^{-1}s^{-1}$. The bunch structure is such that only about 80% of the bunches will be full [9]; given that the total non-diffractive inelastic $p-p$ cross section predicted by PYTHIA is 55 mb, on average 17.3 events will occur at every bunch crossing. With about 50 charged tracks per interaction, this pile-up poses several experimental problems, as discussed in Section 1.2.3.

In the first three years of operation, the LHC will run at a reduced luminosity of $2\times10^{33}cm^{-2}s^{-1}$. The two luminosity regimes are commonly called "High luminosity" and "Low Luminosity", respectively. The LHC will also be able to accelerate and collide beams of heavy ions such as Pb to study the de-confined state of matter, the quark-gluon plasma. The parameters of the LHC are summarised in Table 1.3.

1.2.2 Phenomenology of Proton-Proton Collisions

Protons are not elementary particles, and in high-energy inelastic proton collisions the interaction involves the partons (quarks and gluons) inside the proton. The effective centre-of-mass energy of the hard scattering, $\sqrt{\hat{s}}$, is therefore proportional to the fractional energies x_a and x_b carried by the two interacting partons: $\sqrt{\hat{s}} = \sqrt{x_a x_b s}$, where $\sqrt{s}$ is the centre-of-mass energy of the proton beams.

The momentum distribution of the partons inside the protons are called Parton Density Functions (PDFs). They are different for gluons, u and d valence quarks and low-momentum quark-antiquark pairs of all flavours produced and annihilated as virtual particles (sea quarks). They are functions of the exchanged four-momentum squared, Q^2, since for higher exchanged momenta a shorter distance scale is probed and the contribution of gluons and sea quarks becomes higher. PDFs are obtained from experimental data covering the widest possible range of (x, Q^2); their accuracy is important for several precision measurements. In Fig. 1.4, the CTEQ4M PDFs [10] at two different values of Q^2 are shown.

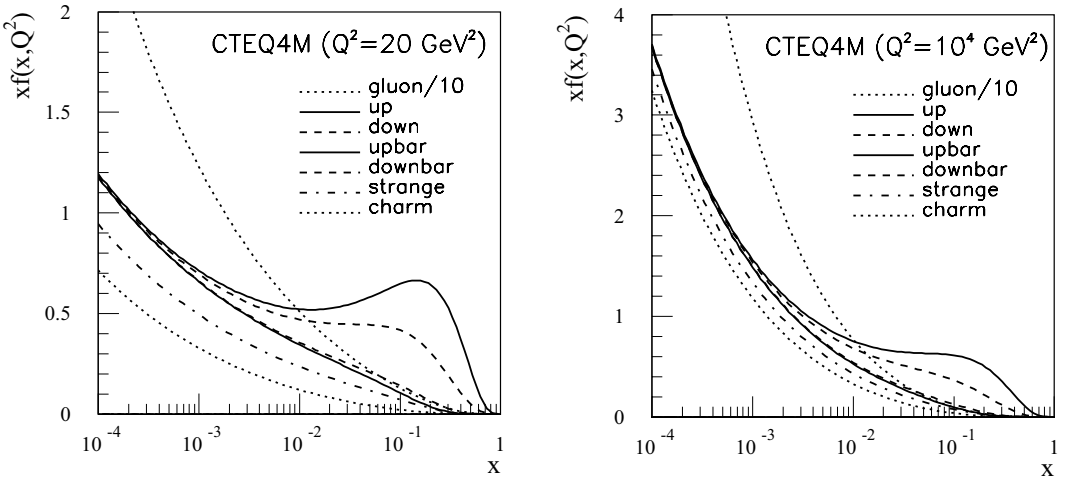

Figure 1.4: *Parton density functions for $Q^2 = 20\ GeV/c^2$ and $Q^2 = 20\ GeV/c^2$ [11].*

The fact that the two partons interact with unknown energies has two fundamental consequences. First of all the total energy of an event is unknown, because the proton remnants, that carry a sizeable fraction of the proton energy, are scattered at small angles and are mostly lost in the beam pipe, escaping detection. Experimentally, it is therefore not possible to define the total and missing energy the event, but only the total and missing transverse energies (in the plane orthogonal to the beams). Moreover, the centre of mass may be

boosted along the beam direction; it is natural to use experimental quantities that are invariant under such boosts, as the transverse momentum p_T. Angular distributions are often described in terms of the *rapidtity*, which is defined choosing the beam direction as z axis:

$$y = \frac{1}{2} \ln \frac{E + p_z}{E - p_z}. \tag{1.11}$$

The rapidity has the property that the shape of dN/dy distributions is invariant under boosts along the z direction. For $p \gg m$ the rapidity is approximated by the *pseudorapidity*:

$$\eta = -\ln \tan \frac{\theta}{2}, \tag{1.12}$$

where θ is the angle between the particle momentum and the z axis. The pseudorapidity has the advantage that it depends only on θ and can be also used for particles of unknown mass.

One very remarkable aspect of LHC physics is the wide cross section range of the processes under investigation: in Fig. 1.3 we see for example that the Higgs production has a cross section at least ten orders of magnitude smaller than the total inelastic cross section. In fact, the bulk of the events produced in proton collisions is either due to low-$\hat{p}_T$ scattering, where the protons collide at large distances, or to QCD high-$\hat{p}_T$ processes of the type:

$$\begin{cases} q_i\bar{q}_i \rightarrow q_k\bar{q}_k \\ q_iq_j \rightarrow q_iq_j \\ q_ig \rightarrow q_ig \\ q_i\bar{q}_i \rightarrow gg \\ gg \rightarrow q_k\bar{q}_k \\ gg \rightarrow gg \end{cases}$$

All these events are collectively called "minimum bias" and in LHC studies are in general considered uninteresting since they constitute a background for other processes, where massive particles like the Higgs are created in the hard scattering. This classification is somewhat arbitrary; for example, this definition of minimum bias events includes $b\bar{b}$ production that is of interest for b-physics studies.

1.2.3 LHC Experiments

LHC detectors will operate in a very difficult environment: the high bunch crossing frequency, the high event rate and the pile-up of several events in the same bunch crossing dictate strict requirements on the design of detectors. To cope with a bunch crossing rate of 25 ns and a pile-up of about 20 events per

crossing, the detectors should have a very fast time response and the readout electronics should also be very fast. Due to the presence of pile-up, high granularity is also required to avoid the overlap of particles in the same sensitive elements. High granularity means a large number of electronics channels, and therefore high cost. LHC detectors will also have to stand an extremely high radiation dose; special radiation-hard electronics must be used.

Additional requirements apply to the online trigger selection, that has to deal with a background rate several orders of magnitude higher than the signal rate. These requirements are discussed in Section 2.5.

Four experiments will be installed at the LHC. Two of them are devoted to specific topics: Alice to heavy ions and LHC-b to b-physics. The other two are the general-purpose experiments ATLAS and CMS. Their design differs significantly, since two very different solutions were chosen for the configuration of magnetic field: CMS uses a solenoidal field generated by a big superconducting solenoid, while ATALS uses a toroidal field produced by three sets of air-core toroids complemented by a small inner solenoid. A detector based on a toroidal magnet has the advantage that the track p_T resolution is constant as a function of pseudorapidity. A very large air-core toroid allows a good momentum resolution even without the aid of the inner tracker; however, it requires very precise detectors with excellent alignment. An iron-core solenoid, on the other hand, can generate a very intense field. The resulting system is very compact and allows calorimeters to be installed inside the magnet, improving the detection and energy measurement of electrons and photons. Precise tracking exploits both the constant field within the magnet and the field inside the return yoke. Moreover, tracks exiting the yoke point back to the interaction point, a property that can be used for track reconstruction. Multiple scattering within the yoke, however, degrades the resolution of the muon system.

Schematic pictures of CMS and ATLAS are shown in Fig. 1.5 and Fig. 1.6, respectively. The CMS experiment is described in detail in Chapter 2.

1.3 Physics with the LHC

Thanks to his high centre-of-mass energy and high luminosity, the LHC has a significant physics potential not only for the discovery of the Higgs, but also in many other fields like electroweak precision measurements, searches and b-physics. In this section, an overview of the LHC physics programme is given.

1.3.1 Higgs Search

In proton-proton collisions, several main processes contribute to the production of the Higgs boson, as illustrated in Fig. 1.7. The cross sections for the

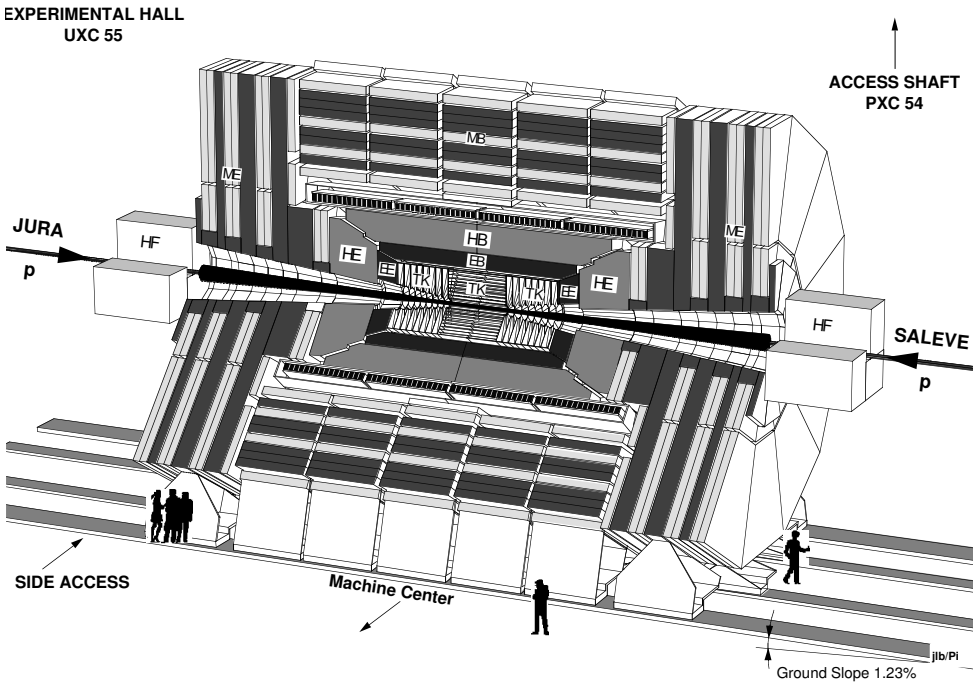

Figure 1.5: *The CMS detector.*

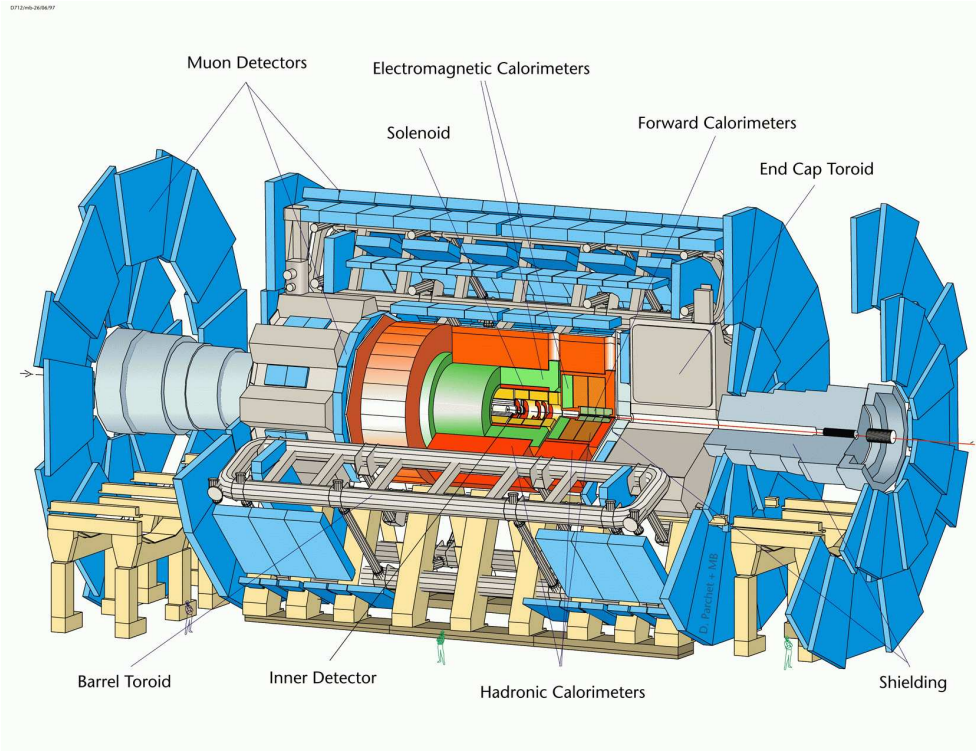

Figure 1.6: *The ATLAS detector.*

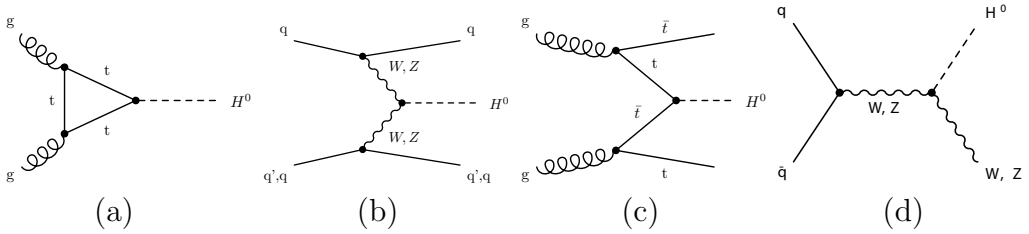

Figure 1.7: *Higgs production mechanisms at tree level in proton-proton collisions: (a) Gluon-gluon fusion; (b) W and Z fusion; (c) $t\bar{t}$ associated production; (d) W and Z associated production.*

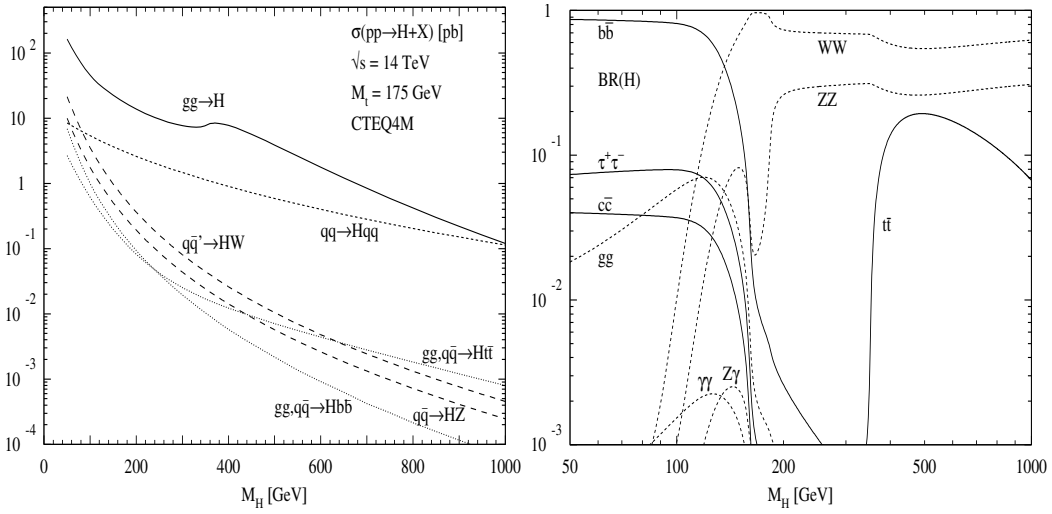

Figure 1.8: *Higgs production cross section (left) and branching ratios (right) as a function of the Higgs mass [12].*

different processes as a function of m_H are shown in Fig. 1.8. Gluon fusion is the dominant process, and only for very high Higgs masses vector does boson fusion become of comparable size. However, the presence of two forward jets is a good experimental signature that can be used to suppress backgrounds. Associated production processes have very small cross sections, except for low Higgs masses; also in this case a powerful signature is given by the additional bosons or quarks in the final state.

Cross sections are of the order of few picobarns, which at the LHC design luminosity correspond to rates of about 10^{-2} Hz. However, not all final states will be experimentally accessible, and the branching ratios of the observable channels are usually small.

The branching ratios for several Higgs decay channels as a function of the Higgs mass are shown in Fig. 1.8. They can be interpreted on the basis of the

Higgs couplings to fermions and gauge bosons:

$$g_{Hff} = \frac{m_f}{v} \tag{1.13}$$

$$g_{HWW} = \frac{2m_W^2}{v} \tag{1.14}$$

$$g_{HZZ} = \frac{m_Z^2}{v}. \tag{1.15}$$

The coupling is proportional to the fermion masses and to the square of the boson masses; therefore the final state with the heaviest available particle dominates. For low Higgs masses ($m_H < 130$ GeV/c^2), the heaviest available fermion is the b quark, and $H \to b\bar{b}$ dominates. However, the QCD jet background is so high at LHC that it will be almost impossible to observe this decay (except maybe by exploiting associated $t\bar{t}H$ or WH production.) The most promising channel is $H \to \gamma\gamma$, which despite the very low branching ratio ($\sim 10^{-3}$) has a very clean signature. The signal should appear as a narrow peak over the continuum $(q\bar{q}, gg) \to \gamma\gamma$ background, but excellent photon energy and angular resolution are required as well as good π^0 rejection.

For larger Higgs masses, the production of WW and ZZ pairs becomes possible; the branching ratio is high, but purely hadronic final states are again not accessible. $H \to 4\ell$ is the "golden-plated" channel for Higgs search; however it has very low branching ratio and suffers from the low Higgs production cross sections above $m_H \sim 600$ GeV/c^2. The channel $H \to WW$ has the disadvantage that accessible final states ($\ell\mu\ell\mu, \ell\nu jj$) have at least one neutrino that escapes detection; however it will be a good discovery channel, especially for $m_H \approx 2m_W$ where the WW production is at threshold and the ZZ branching ratio drops to 20%. For very high Higgs masses (above 500 GeV/c^2), the cross section becomes low and semi-hadronic final states ($2\ell 2j, \ell\nu 2j$) have to be used. The Higgs width becomes also very broad, as shown in Fig. 1.9, so that the reconstruction of a mass peak becomes difficult.

1.3.2 Electroweak Physics

Several precision electroweak measurements will be possible with the two experiments ATLAS and CMS. Thanks to the high statistics available (*e.g.* 10^8 $W \to e\nu$ decays, 10^7 $t\bar{t}$ pairs produced in the first year of operation), for most measurements the statistical uncertainty will be very small. High statistics control samples will allow a good understanding of the detector response, thus reducing the systematic uncertainty.

In the following, we shortly discuss the experimental challenges of some electroweak measurements to be performed at LHC. A more comprehensive discussion can be found elsewhere [8, 13].

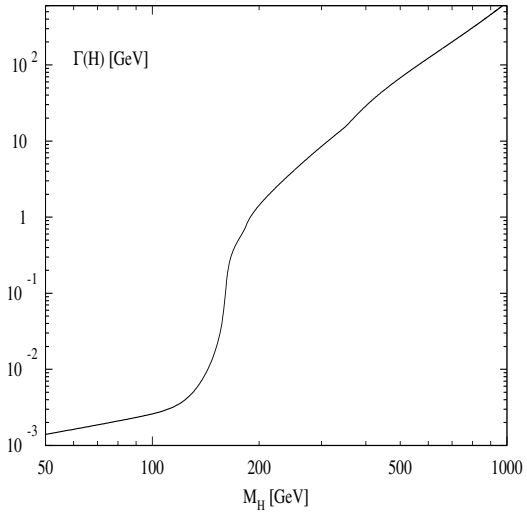

Figure 1.9: *Higgs width as a function of its mass [12].*

1.3.2.1 Measurement of the W and Top Mass

The values of the top and Higgs masses enter in the prediction of the W mass through radiative corrections. Precise measurements of m_t and m_W allow therefore to set limits on m_H and, if the Higgs is found, they will allow stringent tests of the Standard Model (SM) or its extensions like the Minimal Supersymmetric Standard Model (MSSM).

The most promising channel for the measurement of the top mass is $t\bar{t} \to W^+W^-b\bar{b}$ with one leptonic and one hadronic W decay, where the hadronic part is used to reconstruct the top mass and the leptonic part to select the event. The main source of uncertainty will be the jet energy scale, which is affected by the knowledge of fragmentation and gluon radiation and of the response of the detectors. The same sample of $t\bar{t}$ events will provide a large number of hadronic W decays to be used for the calibration of the hadron calorimeters.

The final uncertainty on m_t will be better than about 2 GeV. This will allow to constrain the Higgs mass to better than 30% but, in order not to become the dominant source of uncertainty, the W mass will have be measured with a precision of about 15 MeV.

Since the longitudinal component of the neutrino momentum cannot be measured in hadron colliders, the W mass is obtained from a fit to the distribution of the W transverse mass. The main source of uncertainty is the lepton energy and momentum scale, which should be known with a precision of $\sim 0.02\%$ to achieve the mentioned precision on m_W. This is a challenging goal that could be reached thanks to the high statistics of $Z \to \ell\ell$ decays. Other sources of systematic uncertainty include the W p_T spectrum, the W width and the proton structure functions. Since pile-up deteriorates the shape of the W transverse

mass distribution, this measurement will probably be feasible only in the low luminosity mode.

Several other measurements will be possible in the top quark sector, including rare top decays, the determination of the $t\bar{t}$ production cross section and the observation of single top production.

1.3.2.2 Drell-Yan Production of Lepton Pairs

The Drell-Yan production of lepton pairs is a process with clean signature and low experimental backgrounds. The interesting quantities are the cross section and the forward-backward asymmetry, both functions of the rapidity y and of the invariant mass $m_{\ell\ell}$ of the di-lepton system.

The measurement of the cross section can provide evidence for new physics (new resonances, contact terms etc.) and probe electroweak radiative corrections up to 1.5 TeV. The main issue in this measurement is the knowledge of the absolute luminosity which should reach a precision of 5%, an ambitious goal requiring theoretical improvements in the knowledge of the W and Z production cross section.

The measurement of the forward-backward asymmetry $\mathrm{A_{FB}}$ allows the determination of the effective electroweak mixing angle $\sin^2\theta^{lept}_{eff}$. However, it requires the knowledge of the incoming quark and anti-quark direction, which in $p-p$ colliders is difficult to determine and is affected by the uncertainty on parton density functions. Improving the LEP+SLD accuracy on $\sin^2\theta^{lept}_{eff}$ is therefore a very ambitious goal. Preliminary studies indicate that it might be possible to achieve it if the geometrical acceptance for electrons is extended up to $|\eta| < 4.9$ using the forward calorimeters.

1.3.2.3 Production of Vector Boson Pairs

At the lowest order vector boson pairs are produced in $q\bar{q}$ annihilations followed by triple gauge boson vertices. Triple Gauge Couplings (TGC) allow to test directly the non-Abelian gauge symmetry of the SM. They are described by five parameters, which can be measured with fits to the total cross sections and shapes of distributions such as that of $p_T^{\gamma,Z}$ in Wγ and WZ events. Deviations from the SM values can provide evidence for new physics, *e.g.* the presence of new heavy particles decaying to WW and ZZ pairs (including heavy Higgs). Anomalous couplings are present in many extensions of the SM, including MSSM, technicolour etc. Since the sensitivity to anomalous couplings is enhanced at high centre-of-mass energies, LHC is expected to increase significantly the precision on TGC parameters.

At high energy, the process of vector boson scattering becomes dominant. This process is particularly sensitive to the electroweak symmetry breaking

mechanism and violates unitarity at a scale of ~ 1 TeV. In the SM, this is cured with the introduction of the Higgs boson; in the absence of the Higgs new physics must couple to this channel. Whatever the scenario will be, vector boson scattering will therefore probe the mechanism of electroweak symmetry breaking. It is thus important to measure the WW scattering cross section as a function of the invariant mass of the WW system up to a scale of ~ 1 TeV.

From the experimental point of view, one can exploit the presence of the two quarks emitting the incoming bosons by requiring the signature of forward tagging jets. Other selection criteria are similar to those used for heavy SM Higgs searches. Purely hadronic final states will not be accessible due to the high QCD background; on the other hand it will be useful to reconstruct the invariant mass of the final state boson-boson system also in the absence of a resonance, which is not possible in final states with more than one neutrino.

High integrated luminosities will be necessary for these studies, due to the small cross sections and branching ratios and the high background rates.

1.3.3 Other Physics Studies

Several other topics will be covered by LHC; the most important are mentioned in the following.

Supersymmetry. As already discussed, the simplest supersymmetric model, the Minimal Supersymmetric Standard Model (MSSM), predicts the existence of five Higgs bosons: two charged bosons, $H^{\pm}$, two scalar bosons, h and H, and one pseudo-scalar, A. At tree level, all masses and couplings depend on two parameters, chosen as the mass of the A boson, m_A, and the ratio of the vacuum expectation values of the two Higgs doublets, $\tan\beta$.

In most of the parameter space, charged Higgs bosons decay predominantly to $\tau\nu$. For the neutral Higgs bosons, the decays to vector bosons are suppressed, so that the golden channels described for the case of a SM Higgs will not be observable. The dominant decays modes are those to $b\bar{b}$ and $\tau^+\tau^-$ [12], but the former is hidden by the large background of b-jets. The observation of MSSM Higgs bosons will therefore rely on the identification the leptons coming from τ decays and of τ-jets.

Additionally, supersymmetric theories predict a rich phenomenology. In general supersymmetric particles should be accessible at LHC energies and have very spectacular signatures due to cascade decays with many leptons and jets in the final state and large missing energy. If supersymmetry exists, LHC experiments will certainly be able to observe and study it.

B-Physics. In the field of b-physics, LHC will benefit from a very large $b\bar{b}$ production cross section (see Fig. 1.3). The main interest is the study of the decays of neutral B mesons, and in particular of CP violation in the $B_d^0 - \bar{B}_d^0$ and $B_s^0 - \bar{B}_s^0$ systems. B decays can be identified in leptonic final states, especially in the case of muons. However these leptons are usually soft and the identification is difficult due to the high backgrounds and pile-up. One LHC expriment, LHCb, will be dedicated to b-physics, which will be studied also by ATLAS and CMS will in the low-luminosity phase. At high luminosity, the luminosity in the LHCb collision point will be reduced by de-tuning the beams.

Heavy ions. As already mentioned, LHC will also operate as a collider of heavy ions, with an energy 30 times higher than that that of RHIC, today's most powerful ion collider. Heavy ions collisions will be studied with a dedicated detector, Alice, but also with Atlas and CMS. The goal is to investigate the de-confined state of matter, the quark-gluon plasma.

Chapter 2

The CMS Detector

CMS [14] is a general-purpose detector that will operate at the Large Hadron Collider. The first requirement for CMS was that of a compact design, which leads to the choice of a strong magnetic field (cf. Section 1.2.3). This is obtained using a 4 T superconducting solenoid.

A good and redundant muon system, a good electromagnetic calorimeter and a high quality central tracking are the design priorities of CMS. The CMS solenoid is large enough to accommodate the calorimeters, allowing precision measurements of electrons and photons. The 4 T magnetic field allows precision tracking in the all-silicon inner tracker and reduces the pile-up from soft hadrons in the muon system, which is installed inside the iron return yoke.

This chapter describes the general design of CMS and of its subdetectors. A general description of the CMS trigger system with details on the Level-1 trigger is given in Section 2.5.

2.1 Overall Design

The CMS detector is composed of a cylindrical barrel closed by two endcap disks, with a full length of 21.6 m, a diameter of 15 m and a total weight of $\sim$ 12500 tonnes.

The longitudinal view of one quarter of the CMS detector is shown in Fig. 2.1. The transversal view of the barrel region is shown in Fig. 2.2. Detectors and non-sensitive volumes are indicated with standard two-letter codes (the second being `B` for barrel and `E` for endcap) which will be used in the following.

The CMS coordinate frame is a right-handed system where the x axis points to the centre of the LHC ring, the z axis is parallel to the beam and the y axis points upwards. Reconstruction algorithms however use a spherical coordinate system based on the distance r from the z axis, the azimuthal angle ϕ with respect to the y axis and the pseudo-rapidity η defined in Eq. 1.12.

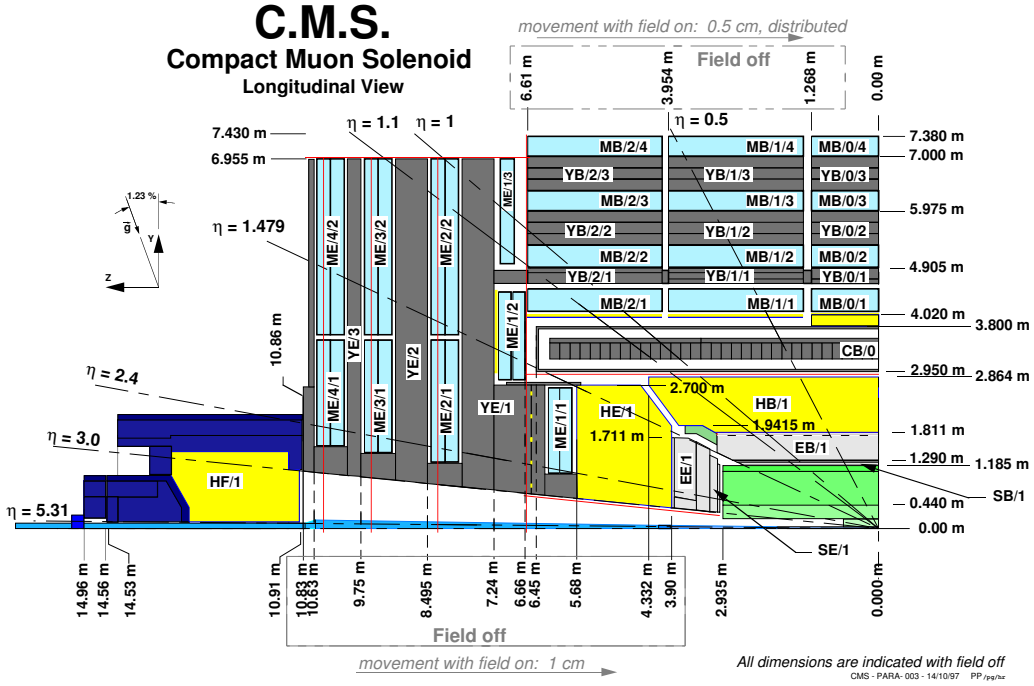

Figure 2.1: *Longitudinal view of one quarter of the CMS detector.*

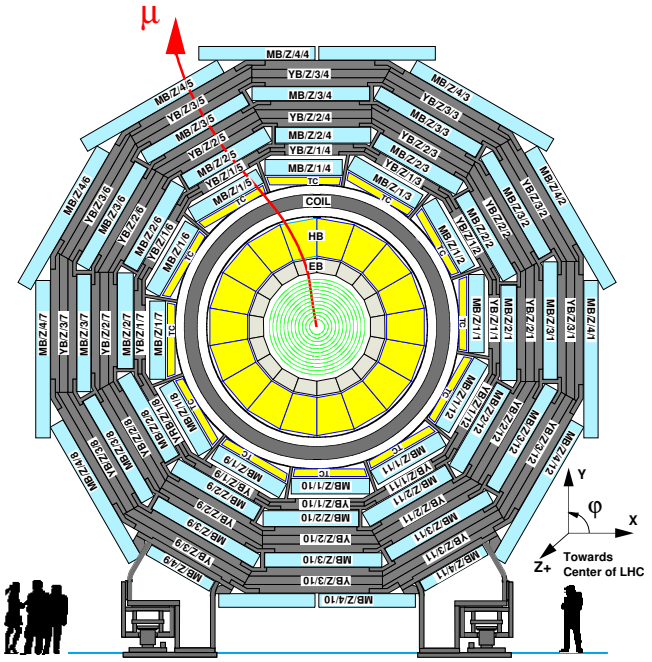

Figure 2.2: *Transverse view of the barrel region of the CMS detector. Barrel wheels are numbered Z = -2, -1, 0, 1, 2.*

The CMS design is driven by the choice of its magnet (CB), a 13 m long superconducting solenoid [15] with a diameter of 5.9 m. Cooled with liquid helium, it will generate a magnetic field of 4 T, which is kept uniform by a massive iron return yoke (YB,YE). The yoke will also host the muon system (MB,ME), composed by drift tube detectors in the barrel region and cathode strip chambers in the endcaps (up to $|\eta| < 2.4$), complemented by a system of resistive plate chambers with a coverage of $|\eta| < 2.1$. The muon system is described in detail in Section 2.4.

The calorimeters and the inner tracker are installed inside the coil. The innermost tracking detector is essential for precise vertex reconstruction and b-tagging and has to deal with a very high track density. Very fine segmentation is crucial; therefore a silicon pixel detector was chosen. In the baseline design it consists of 3 barrel layers and 2 forward disks. Outside the pixel detector, a silicon strip detector is installed, extending up to a radius of about 1.2 m. The full silicon tracker allows charged tracks reconstruction with at least 12 measurement points and a coverage of $|\eta| < 2.5$; it is described in Section 2.2.2.

Photons and electrons are measured by a homogeneous electromagnetic calorimeter (ECAL), composed by $PbWO_4$ scintillating crystals covering the region $|\eta| < 3.0$ (EB,EE). In the endcaps, it will be supplemented by a lead/silicon preshower detector, to improve the resolution in the determination of electron and photon direction and help pion rejection. The ECAL is described in Section 2.3.

Jets and energy imbalance are measured by a sampling hadronic calorimeter (HCAL) installed just before the coil. It is composed of a copper alloy and stainless steel instrumented with plastic scintillators. The barrel and endcap parts (HB,HE) have the same $|\eta|$ coverage as the ECAL, and are complemented by a very forward calorimeter (HF), which extends the coverage up to $|\eta| < 5.3$, enhancing the hermeticity of the detector and its ability to measure missing transverse energy. The HCAL is described in Section 2.3.1.

2.2 The Tracker

The goal of the inner tracker [16, 17] is to reconstruct high-p_T charged tracks in the region $|\eta| < 2.5$ with high efficiency and momentum resolution, to measure their impact parameter and to reconstruct secondary vertices. This is obtained with a detector based on several layers of silicon detectors. The first layers, which are closer to the interaction point, are crucial for the measurement of the impact parameter, and have to cope with a very high particle flux. Finely segmented pixel detectors are used in this region. The rest of the tracker is composed of single-sided and double-sided silicon strip detectors extending up to $r = 110$ cm and $|z| = 270$ cm. The pixel and silicon detectors are described

in Section 2.2.1 and Section 2.2 respectively.

2.2.1 The Pixel Detector

The pixel detector will provide high-resolution three-dimensional measurements, that will be used for charged track reconstruction. Its excellent resolution will also allow the measurement of track impact parameters, the identification of b- and τ-jets and the reconstruction of vertices in three dimensions. It consists of square n-type silicon pixels with a size of 150 μm $\times$150 μm on a n-type silicon substrate. A spatial resolution of $\sim$ 15 μm is obtained by analogic interpolation of the charge induced in nearby pixels, helped by the large Lorentz drift angle in the magnetic field. Charge sharing is enhanced in the endcaps by tilting the detectors by 20^0. The full detector consists in a total of 4.4 million pixels.

The baseline design of the pixel detector includes three barrel layers at mean radii of 4.4 cm, 7.3 cm and 10.2 cm, extending for a total length of 53 cm. Two endcap disks, extending in radius from 6 to 15 cm, will be placed on each side at z=34.5 cm and 46.5 cm. A three-dimensional representation of the pixel detector is shown in Fig. 2.3. This layout will guarantee at least two pixel hits

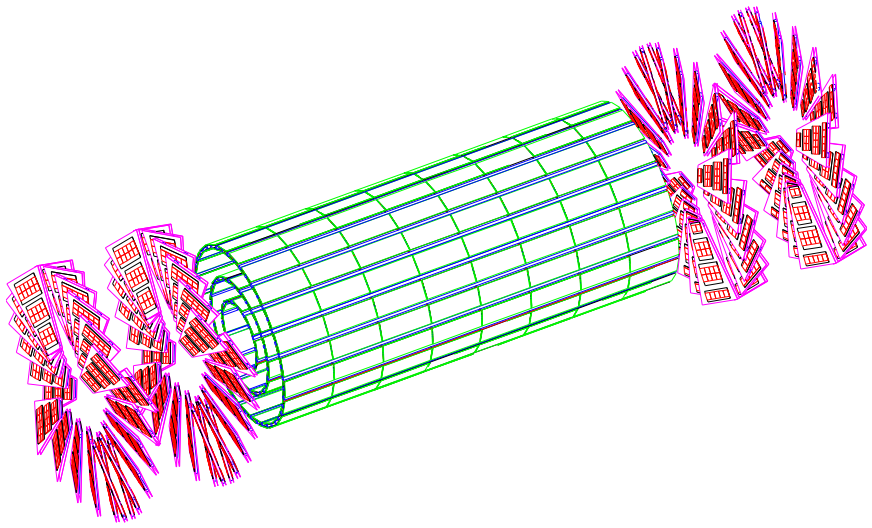

Figure 2.3: *Three-dimensional view of the full pixel detector.*

for tracks originating within $2\sigma_Z$ from the nominal collision point, up to about $|\eta| < 2.2$. Standalone track reconstruction, that requires three hits per track, will also be possible, with good efficiency in the same region. However, in the initial low-luminosity phase only two barrel layers and one end-cap disk will be installed. Standalone track reconstruction will not be possible in this case, and two-hit coverage will be limited to $|\eta| < 2.0$.

The large particle flux imposes also special requirements of radiation hardness, and it is very likely that the pixel detectors will have to be substituted during the lifetime of the experiment.

2.2.2 The Silicon Microstrip Detector

In addition to the pixel detectors, the inner tracker is composed of several layers of silicon microstrip detectors, whose layout is shown in Fig. 2.4. The inner part consists of four barrel layers and three small forward disks. The outer part consists of six barrel layers and nine forward disks.

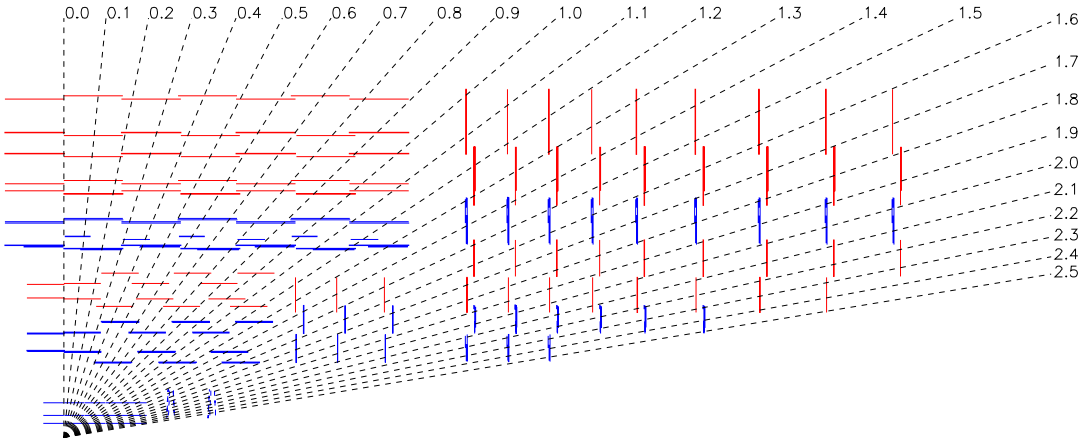

Figure 2.4: *Longitudinal view of one quarter of the silicon tracker, including the pixel detector.*

The full tracker consists of about 15000 microstrip detectors, with a pitch size ranging from about 80 to 180 μm. Some of the modules are composed by two detectors mounted back-to-back with the strips rotated by 100 mrad. These double-sided ("stereo") modules will also provide a measurement in the coordinate orthogonal to the strips.

The resolution of the full non-staged tracker for the measurement of the transverse momentum and the transverse impact parameter are shown in Fig. 2.5.

2.3 The Electromagnetic Calorimeter

The goal of the electromagnetic calorimeter (ECAL) [18] is the accurate measurement of the energy and position of electrons and photons. Its design is driven by the requirement of a 1% two-photon invariant mass resolution, in

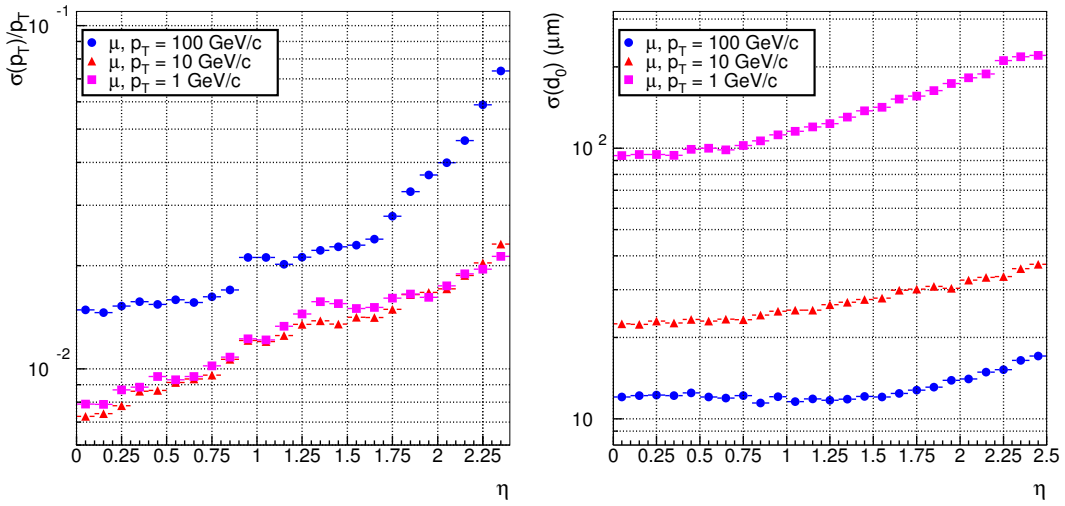

Figure 2.5: *Resolution of the tracker on the transverse momentum (left) and the transverse impact parameter (right) as a function of pseudorapidity, for single muons with transverse momentum of 1, 10 and 100 GeV/c [1].*

order to allow the observation of a low-mass Higgs in the $\gamma\gamma$ channel. A homogeneous calorimeter has therefore been chosen, composed of about 80000 finely segmented lead tungstate ($PbWO_4$) crystals. Lead tungstate is a fast, radiation-hard scintillator characterised by a small Molière radius (21.9 mm) and a short radiation length (8.9 mm), that allows good shower containment in the limited space available for the ECAL.

The length of the crystals is 230 mm in the barrel and 220 mm in the endcaps, corresponding to 25.8 and 24.7 radiation lengths respectively. Crystals are trapezoidal, with a square front face of 22×22 mm^2 in the barrel and 30×30 mm^2 in the endcaps, matching the Molière radius. Scintillator light is collected by silicon avalanche photo-diodes in the case of barrel crystals, and vacuum photo-triodes for endcaps crystals.

A preshower detector is installed in front of the endcaps, consisting of two lead radiators and two planes of silicon strip detectors, with a total radiation length of 3 X_0. It will allow rejection of photon pairs from π^0decays and improve the estimation of the direction of photons, to improve the measurement of the two-photon invariant mass.

The longitudinal view of one quarter of the ECAL is shown in Fig. 2.6. The geometric coverage extends up to $|\eta| = 3.0$.

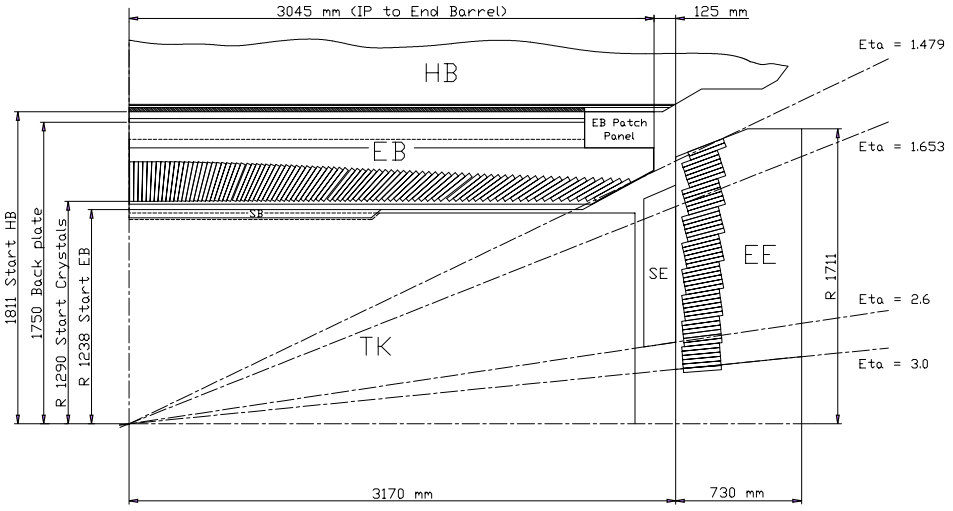

Figure 2.6: *Longitudinal view of one quarter of the ECAL.*

The energy (E) resolution of a calorimeter can be parametrised as

$$\left(\frac{\sigma}{E}\right)^2 = \left(\frac{a}{\sqrt{E}}\right)^2 + \left(\frac{\sigma_n}{E}\right)^2 + c^2 \tag{2.1}$$

where a is called stochastic term and includes the effects of fluctuations in photo-statistics as well as in the shower containment, σ_n is the noise from the electronics and pile-up and c is a constant term related to the calibration of the calorimeter. The different contributions are shown in Fig. 2.7.

2.3.1 The Hadron Calorimeter

The goal of the hadron calorimeter (HCAL) [19] is is to measure the direction and energy of jets, the total transverse energy and the imbalance in the transverse energy (missing E_T). High hermeticity is required for this purpose. For this reason, the barrel and endcap parts installed inside the magnet are complemented by a very forward calorimeter which is placed outside the magnet return yokes, with a total coverage of $|\eta| < 5.3$.

The barrel and endcap HCAL cover the region $|\eta| < 3.0$. They are sampling calorimeters, whose active elements are plastic scintillators interleaved with brass absorber plates and read out by wavelength-shifting fibres. The first layer is read out separately, while all others are read out together. Both barrel and endcap are read-out in towers with a size of $\Delta\eta \times \Delta\phi = 0.087 \times 0.087$. In the barrel, full shower containment is not possible within the magnet volume, and an additional "tail catcher" is placed outside the magnet. The very forward

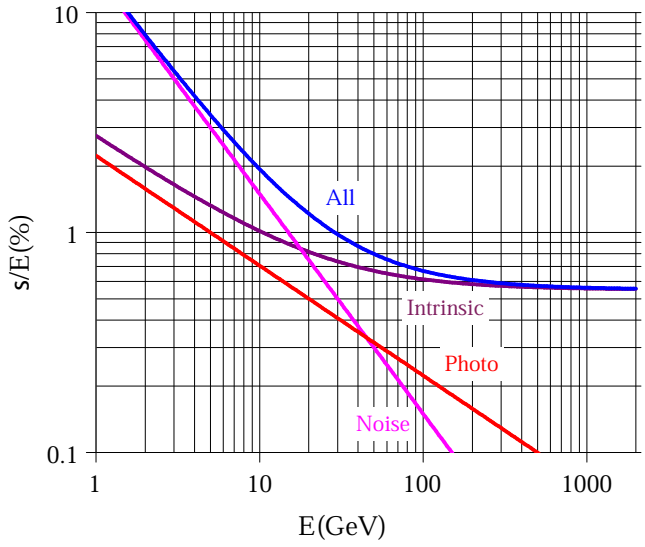

Figure 2.7: *Different contributions to the energy resolution of the ECAL [18]. The curve labelled "intrinsic" includes the shower containment and a constant term of 0.55%.*

calorimeter is placed outside the magnet yoke, 11 m from the interaction point. The active elements are quartz fibres parallel to the beam, inserted in steel absorber plates.

The energy resolution is $\sigma/E \sim 65\%\sqrt{E}\oplus 5\%$ in the barrel; $\sigma/E \sim 85\%\sqrt{E}\oplus$ 5% in the endcaps and $\sigma/E \sim 100\%\sqrt{E} \oplus 5\%$ (E in GeV) in the very forward calorimeter.

2.4 The Muon System

The goal of the muon system [20] is to identify muons and allow, in combination with the inner tracker, an accurate measurement of their transverse momenta. High-p_T muons provide a clean signature for many physics processes; therefore the muon system plays an important role in the trigger.

The muon system, shown in Fig. 2.8, is embedded in the iron return yoke of the magnet, which shields the detectors from charged particles other than muons. The magnetic field inside the plates of the yoke bends the tracks and allows the measurement of their p_T.

The muon system consists of three independent subsystems. In the barrel, where the track occupancy and the residual magnetic field are low, drift tube detectors (DT) are installed. In the endcaps, cathode strip chambers (CSC) are used, since detectors in this region have to cope with high particle rates and large residual magnetic field between the plates of the yoke. The DT and CSC

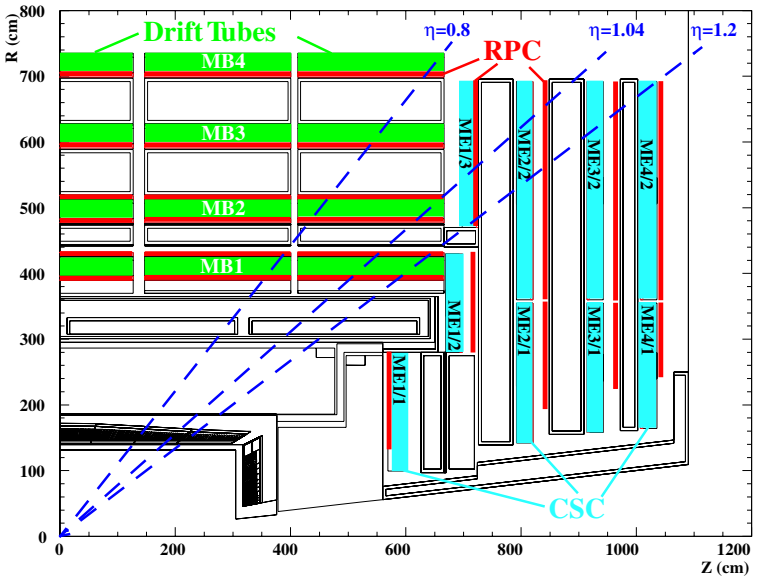

Figure 2.8: *Longitudinal view of one quarter of the muon system.*

systems cover the region $|\eta| < 2.4$. Redundancy is obtained with a system of resistive plate chambers (RPC), that are installed in both the barrel and the endcaps. RPCs have limited spatial resolution, but fast response and excellent time resolution, providing unambiguous bunch crossing identification. They are also used to complement DTs and CSCs in the measurement of the p_T. The RPC system covers the region $|\eta| < 2.1$.

2.4.1 The Drift Tube Chambers

Muon detectors in the barrel do not operate in particularly demanding conditions, since the occupancy in this region is low and the magnetic field is well contained in the iron plates of the return yoke. For this reason, drift tubes were chosen. The chamber segmentation follows that of the iron plates of the yoke, consisting in five wheels along the z-axis, each one divided in 12 sectors. Chambers are arranged in four *stations*, *i.e.* concentric cylinders, named MB1,...,MB4 as shown in Fig. 2.8. Each station consists of 12 chambers, except for MB4 where 14 chambers are present.

The basic detector element is a drift tube cell, whose section is shown in Fig. 2.9. Cells have a size of 42×13 mm. A layer of cells is obtained by two parallel aluminium planes and by "I" shaped aluminium beams which define the boundary of the cells and serve as cathodes. I-beams are insulated from the planes by a 0.5 mm thick plastic profile. The anode is a 50 μm stainless steel

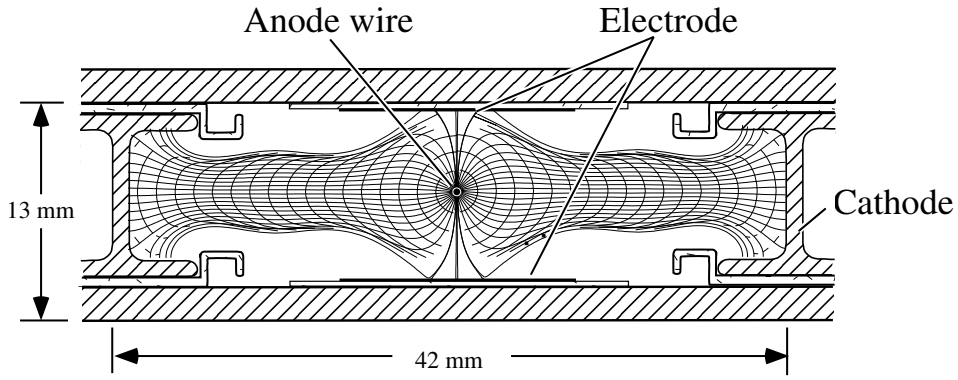

Figure 2.9: *Section of a drift tube cell.*

wire placed in the centre of the cell. The distance of the track from the wire is measured by the drift time of electrons; to improve the distance-time linearity, additional field shaping is obtained with two positively-biased insulated strips, glued on the the planes in correspondence to the wire. Typical voltages are +3600 V, +1800 V and -1200 V for the wires, the strips and the cathodes, respectively. The gas is a 85%/15% mixture of Ar/CO_2, which provides good quenching properties and a saturated drift velocity, of about 5.6 cm/μs. The maximum drift time is therefore $\sim$ 375 ns, *i.e.* 15 bunch crossings. A single cell has an efficiency of about 99.8% and a resolution of $\sim$ 180 μm.

Four staggered layers of parallel cells constitute a *super-layer*, which allows to resolve the left-right ambiguity of a single layer and provides the measurement of a two-dimensional segment. Also, it measures the bunch crossing originating a segment with no need of external input, using a generalisation of the mean-timer technique [21].

A chamber is composed by two super-layers measuring the $r-\phi$ coordinates, with the wires parallel to the beam line, and an orthogonal super-layer measuring the $r-z$ coordinates. The latter is not present in the outermost station (MB4). A cross-sectional view of a chamber is shown in Fig. 2.10.

2.4.2 The Cathode Strip Chambers

Cathode strip chambers are multi-wire proportional chambers with good spatial and time resolution, that can operate at high occupancy levels and in the presence of a large inhomogeneous magnetic field. For this reason they were adopted in the endcap region.

CSC chambers are arranged in four disks (*stations*) placed between the iron disks of the yoke and labelled ME1,...,ME4 (cf. Fig. 2.8). The innermost

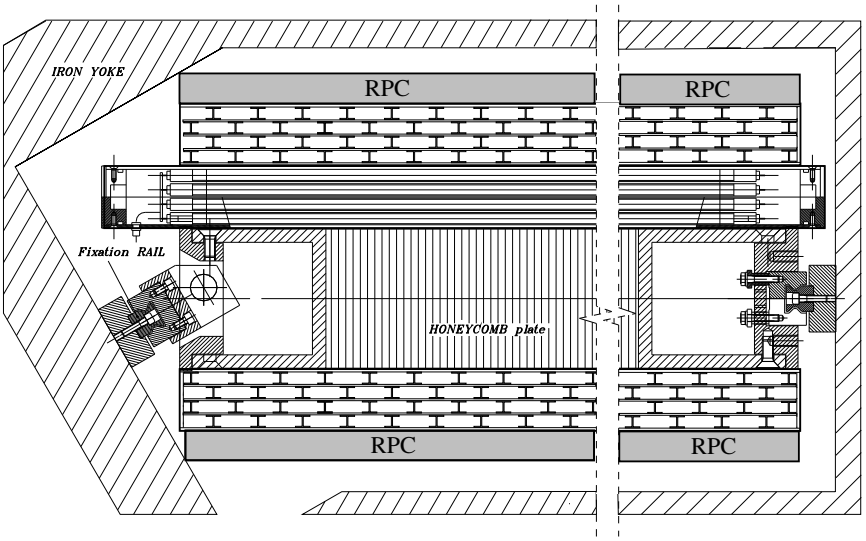

Figure 2.10: *Schematic view of a MB1/MB2 DT chamber, with two attached Resistive Plate Chambers.*

station consists of three concentric rings, the first (ME1/1) being closer to the interaction point than the other two. The other stations are composed by two disks only. The rings are formed by 18 or 36 trapezoidal chambers, which, with the exception of the outermost ring of ME1, are staggered with a small overlap in ϕ.

Chambers are composed of six layers, each consisting of an array of anode wires between two cathode planes (see Fig. 2.11). The gap is 9.5 mm thick and is filled with a 30%/50%/20% mixture of $Ar/CO_2/CF_4$. One of the two cathode planes is segmented into strips orthogonal to the wires. The avalanche produced in the gap by a crossing charged particle induces a charge in several adjacent strips, and an interpolation of the signals gives a precise spatial measurement.

Strips are radial and measure the ϕ coordinate. The orthogonal coordinate (r) is measured by the wires which, to reduce the number channels, are read out in groups of 5 to 16. The resolution is of the order of ~ 0.5 cm, to be compared with ~ 50 μm of the strip measurement.

The first disk of ME/1 has to operate in difficult conditions, as it is exposed to a high magnetic field and particle rate. A slightly different design is adopted for chambers in this disk, with wires tilted by 25° to compensate for the Lorentz drift in the magentic field. The gap is reduced to 6 mm and the number of strips is doubled above $\eta = 2.0$.

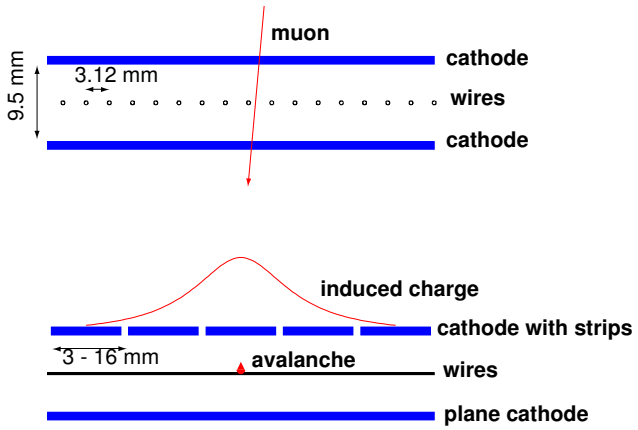

Figure 2.11: *Orthogonal sections of one CSC layer.*

2.4.3 The Resistive Plate Chambers

The RPC system is complementary to the DT and CSC systems, and adds robustness and redundancy to the muon trigger. Resistive plate chambers provide limited spatial resolution, but excellent time resolution, of the order of few nanoseconds.

In the barrel, RPC chambers follow the segmentation of DT chambers. A total of six layers of RPCs are present; the first four are attached to each side of the MB1 and MB2 DT chambers, as shown in Fig. 2.10. The other two are attached to MB3 and MB4. In the endcaps, chambers are trapezoidal; four layers are present.

The resistive plate chambers used in CMS are composed of four bakelite planes forming two coupled gaps, as shown in Fig. 2.12. The gaps are filled with a mixture of 90% $C_2H_2F_4$ (freon) and 5% i-C_4 H_{10} (isobutane). The planes are externally coated by graphite electrodes, the two innermost ones set to +9.5 kV. Insulated aluminium strips are placed in the middle, to collect the signal induced by crossing particles. This two-gap design is adopted to increase the charge induced on the strips.

In the barrel, the strips are parallel to the beam line, with a length of 80 or 120 cm. In the endcap, strips are radial with a length of 25 to 80 cm. The coordinate orthogonal to the strips is estimated as the centre of a cluster of fired adjacent strips. No measurement is available in the second coordinate, apart from the constraint coming from the strip length.

RPCs will operate in "avalanche" mode rather than in the more common "streamer" mode. This is obtained with a lower electric field, and allows to sustain higher rates. However, the gas multiplication is reduced, and improved

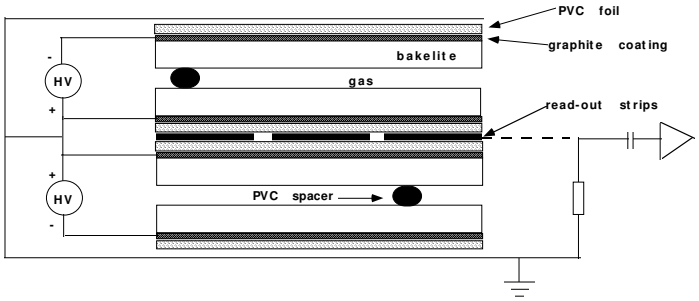

Figure 2.12: *Schema of a double-gap resistive plate chamber.*

electronic amplification is required.

RPC detectors constitute an effective and cheap alternative to scintillators. However, there are concerns about the noise rate due to discharges caused by irregularities in the bakelite surfaces. These effects can be suppressed by treating the surfaces with lineseed oil, which has been adopted for the barrel detectors. However, the high radiation dose can cause aging effects on the oil, which is therefore not used in the endcaps.

2.5 The CMS Trigger

At the LHC nominal luminosity, the total event rate is of the order of 10^9 Hz; however, the rate for interesting events is very small, as shown in Fig. 2.13. A large fraction of the corresponding selection has to be performed on-line, since the raw event size is of the order of 1 MB and storing and processing the resulting amount of data would be prohibitively difficult and expensive. The goal of the trigger system is to perform this online selection, reducing the event rate to the order of 100 Hz, that is enough to accommodate the signal channels of interest at LHC. This task is difficult not only due to the high rejection factors it requires ($\sim 10^7$), but also because the output rate is saturated already by processes like $Z \to \ell\ell$ and $W \to \ell\nu$, where high-p_T leptons are produced. The trigger must therefore be able to select events on the basis of their physics, and online selection algorithms must have a level of sophistication comparable to that of offline reconstruction.

Moreover, the time available to perform this selection is limited. Bunch crossings will occur at a rate of 40 MHz, so that a decision must be taken every 25 ns. This time is too small even to read out all raw data from the detector. The accept/reject decision will be taken in several steps (levels) of increasing refinement, where each one takes a decision using only part of the available data.

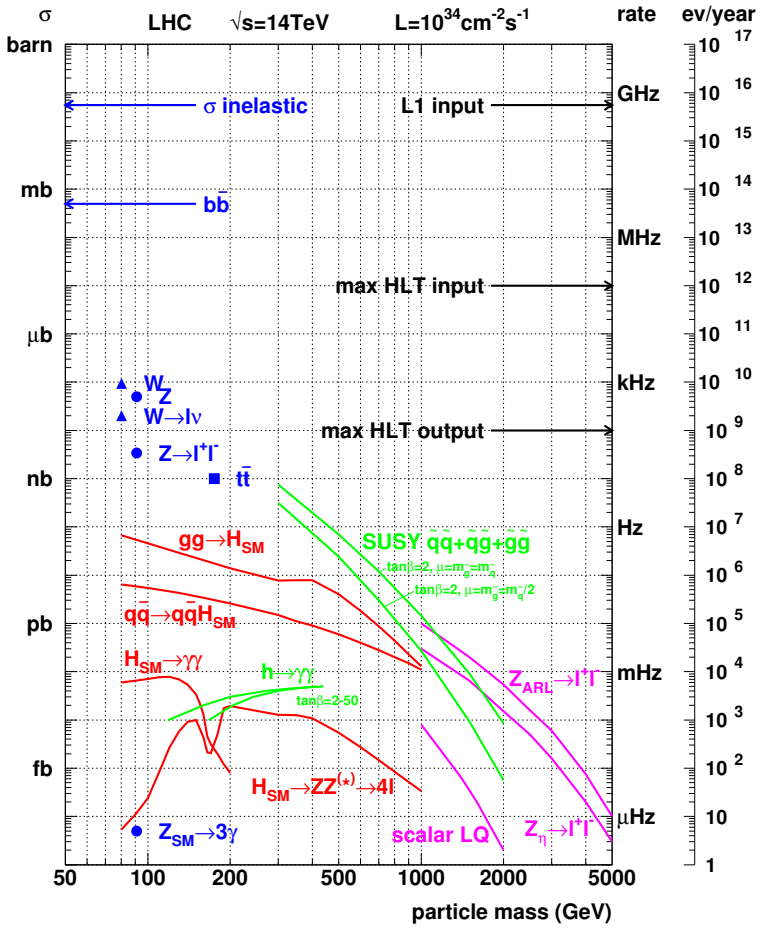

Figure 2.13: *Cross section and event rates at* $10^{34} cm^{-2} s^{-1}$ *as a function of the mass of produced objects [Courtesy G. Wrochna].*

In this way, higher trigger levels have to process fewer events and have more time available; they can go into finer detail and use more refined algorithms.

Due to the strict timing constraints, the first step of the CMS trigger, the Level-1 trigger, is implemented on dedicated programmable hardware. The Level-1 has access to the data from the calorimeters and the muon detectors with coarse granularity; on the basis of this limited information it has to reduce the input rate up to a level acceptable for the Data Acquisition system (DAQ). At startup, the DAQ system will be able to handle an event rate of up to 50 kHz, which will be increased to 100 kHz when the full LHC design luminosity is reached. Only one third of this bandwidth is allocated, the rest being used as safety margin accounting for all uncertainties in the simulation of the basic physics processes. The allocation of this bandwidth among different triggers is discussed in Section 2.5.1.4.

The selected events are passed to the High Level Trigger (HLT), which will be completely implemented on software running on a farm of commercial processors. This allows full flexibility and optimisation of the algorithms. The HLT is further subdivided in logical levels (Level-2, Level-3), although this classification is somewhat arbitrary. The implementation and performance of the muon HLT algorithms is described in Chapter 4.

The following sections briefly describe the design of the Level-1 trigger, with particular focus on the muon trigger. A more detailed discussion can be found elsewhere [22].

2.5.1 The Level-1 Trigger

The Level-1 trigger [22] is implemented on custom-built programmable hardware. It runs dead-time free and has to take an accept/reject decision for each bunch crossing, i.e. every 25 ns. This is achieved with a synchronous pipelined structure of processing elements, each taking less than 25 ns to complete. At every bunch crossing, each processing element passes its results to the next element and receives a new event to analyse. During this process, the complete detector data are stored in pipeline memories, whose depth is technically limited to 128 bunch crossings. The Level-1 decision is therefore taken after a fixed time of 3.2 μs. This time must include also the transmission time between the detector and the counting room (a cable path of up to 90 m each way) and, in the case of Drift Tube detectors, the electron drift times (up to 400 ns). The time available for calculations can therefore be as low as 1 μs.

The Level-1 trigger is divided in three subsystems: the Calorimeter Trigger, the Muon Trigger and the Global Trigger. The Muon Trigger is further subdivided in three independent systems for the DTs, CSCs and RPCs, respectively. The results of these three systems are combined by the Global Muon Trigger. A schematic view of the components of the Level-1 trigger system and of their relationships is shown in Fig. 2.14.

The Calorimeter and Muon Triggers do not perform any selection themselves. They identify "trigger objects" of different types: isolated and non-isolated electrons/photons; forward, central and τ-jets; and muons. The four best candidates of each type are selected and sent to the Global Trigger, together with the measurement of their position, transverse energy or momentum and a quality word. The Global Trigger also receives the total and missing transverse energy measurement from the Calorimeter Trigger.

The Global Trigger selects the events according to programmable trigger conditions, that can include requirements on the presence of several different objects with energies or momenta above predefined thresholds. Topological conditions and correlations between objects can be required as well. Up of 128 of these conditions can be tested in parallel, and each can be pre-scaled to

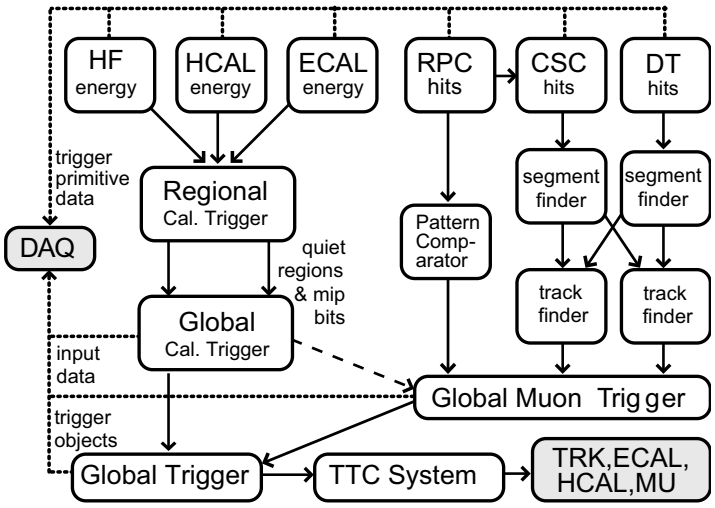

Figure 2.14: *Structure of the Level-1 trigger system.*

accept only a fraction of selected events.

The Level-1 Calorimeter and Muon Triggers are shortly described in the following. A more detailed discussion is outside the scope of this work, and the interested reader is referred to more specific publications [22].

2.5.1.1 The Level-1 Calorimeter Trigger

The calorimeter trigger identifies five types of objetcs: isolated electrons/photons, non-isolated electrons/photons, central jets, forward jets and tau jets. The measurement of the transverse energy and position of the four most energetic objects of each type is sent to the Global Trigger, together with a measurement of the total and missing transverse energy. In addition, the calorimeter trigger provides the Muon Trigger information about the activity in all calorimeter regions, to determine if the energy deposit is compatible with the passage of a muon (MIP bit) and if it is below a programmable threshold (Quiet bit).

For trigger purposes, the calorimeters are subdivided in towers with a size of $\Delta\phi \times \Delta\eta = 0.087 \times 0.087$ up to $\eta \sim 2$. At higher pseudorapidity values $\Delta\eta$ increases up to 0.35. Trigger towers match the granularity of HCAL up to $\eta > 1.74$; above that value, physical HCAL towers have twice the ϕ dimension of the trigger tower. In the barrel ECAL, each tower corresponds to 5×5 crystals, while the ECAL endcap crystals are arranged in a $x - y$ geometry, and a variable number of crystals is grouped, matching as much as possible the HCAL trigger tower boundaries. Towers are defined also in the very forward calorimeter, with a size of $\Delta\phi \times \Delta\eta = 0.348 \times 0.5$.

The trigger towers are organised in calorimeter regions, each formed by 4×4 trigger towers, with a size of about $\Delta\phi \times \Delta\eta = 0.35 \times 0.35$. Very forward calorimeter towers constitute a region by themselves, due to their size.

The data of each ECAL and HCAL trigger tower is first processed by the Trigger Primitive Generator, which is integrated in the calorimeter readout electronics. It provides bunch crossing identification based on a peak-finder algorithm, and for each tower calculates the so-called trigger primitives, *i.e.* the sum of the transverse energy and a fine grain bit. The ECAL fine grain bit provides information on the lateral extension of the electromagnetic shower, and is used in the rejection of backgrounds by the electron trigger. The HCAL fine grain bit is used to denote the compatibility of the deposit with the passage of a minimum ionising particle, and is set if the HCAL energy before conversion to the transverse scale is within a programmable range, of the order of [1.5, 2.5] GeV.

The trigger primitives are used by the different calorimeter trigger algorithms described in the following.

Photon and electron trigger. At Level-1, it is not possible to distinguish electrons and photons, which are treated together. Electron/photon candidates are found with a sliding window algorithm on 3×3 towers. Identification is based on the presence of a large energy deposition in one or two adjacent trigger towers. Requirements on the lateral and longitudinal profile of the shower are also set using the ECAL fine grain bit and the ratio of ECAL and HCAL energy deposits, respectively. A candidate is labelled isolated on the basis of the energy deposits and ECAL fine grain bits in the eight towers around the centre of the 3×3 window.

In each calorimeter region, the highest-E_T isolated and non-isolated candidates are found. The Global Calorimeter Trigger sends the four most energetic ones of each type to the Global Trigger.

Jets and τ-jets. The jet trigger uses the sum of the ECAL and HCAL transverse energies in calorimeter regions. Candidates are found with a sliding window algorithm on 3×3 regions, requiring the deposit in the central one to be higher than the deposits in the other eight.

Additionally, τ-jets are identified by their narrow profile. A jet candidate is identified as τ-jet if each of the nine regions of the window contains no more than two towers above a programmable threshold.

Jets are searched for separately in the central region ($|\eta| < 3$) and in the forward region ($3 < |\eta| < 5$), while τ jets are only identified in the central one. The Global Calorimeter Trigger sends the four most energetic candidates of each type to the Global Trigger, together with the number of jets above a

programmable threshold.

Total and missing transverse energy. The total energy is obtained by summing the transverse energy of all ECAL and HCAL calorimeter regions. The missing transverse energy is determined from the sum of the E_x and E_y components of the deposit in each region, obtained from the E_T deposits using the coordinates of the centre of the region. The total and the missing energy (absolute value and ϕ direction) are then sent to the Global Trigger.

Quiet and MIP bits. For each calorimeter region, a "Quiet" bit is defined if the transverse energy deposit in ECAL plus HCAL is below a programmable threshold. The MIP (Minimum Ionising Particle) bit is set if the quiet bit is set and if the HCAL fine grain bit is set in at least one of the 16 HCAL towers of the region. These two bits can be used by the Global Muon Trigger to select muons, as described in Section 5.1.

2.5.1.2 The Level-1 Muon Trigger

The Muon Trigger has the task to identify muons, reconstruct their position and transverse momentum and provide bunch crossing assignment with high purity and efficiency. It is described in detail in [22]. The most relevant change from what described therein is that the trigger electronics will not be installed in the forward CSC station ME1/1a, thus limiting the Level-1 trigger acceptance to $|\eta| < 2.1$ (see below).

All three detector systems described in Section 2.4 contribute to the muon trigger, which benefits from the complementary characteristics of these systems: the good spatial resolution of drift tubes and cathode strip chambers and the excellent time resolution of resistive plate chambers. The redundancy of the muon system allows a robust trigger with high efficiency and good background rejection. The wire chamber systems and the RPC system are complementary in performance and also in the backgrounds and inefficiencies they are sensitive to. The complementarity can also be used for cross-checks and to improve the understanding of the performance of each system.

The internal structure of the Muon Trigger is shown in Fig. 2.15. In the case of DTs and CSCs, the information of each chamber is first processed independently by a Local Trigger step, where track segments are reconstructed. Segments of the different stations are matched by the DT and CSC Regional Track Finders, which reconstruct muon tracks and estimate their p_T. The candidates found are then delivered to the Global Muon Trigger, with a word to indicate their quality. In the overlap region, DT and CSC segments are used by both Track Finders to allow for reconstruction of full tracks in each of the two subsystems.

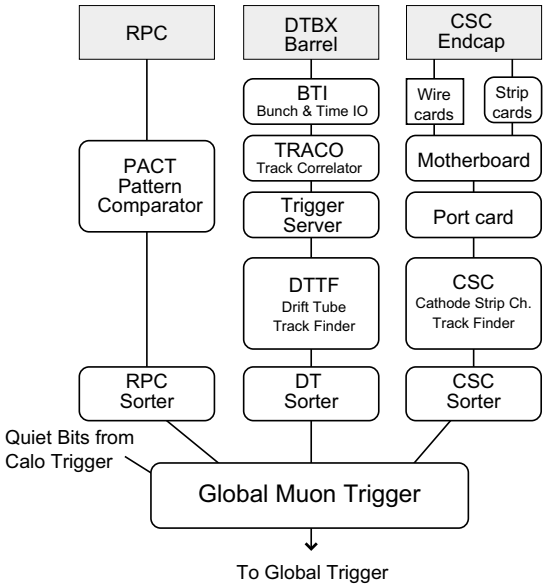

Figure 2.15: *Schematic structure of the muon trigger system.*

In the case of RPCs, the hits are collected by a Pattern Comparator Trigger (PACT), which looks for predefined patterns. The PACT provides an estimate of the p_T of the muon and its position, as well as a word to indicate its quality.

Each subsystem reconstructs up to four muon candidates. These are sent to the Global Muon Trigger that matches them and looks for the MIP and Quiet bits in the corresponding calorimeter regions. Finally, the four muons with highest p_T are sent to the Global Trigger. The track reconstruction in the different subsystems is shortly described in the following.

The DT Trigger. The DT trigger front-end is called Bunch and Track Identifier (BTI). It is directly connected to the read-out electronics, and performs a straight segment fit within a superlayer using at least three hits out of the four layers of drift cells. The fit is done with a generalisation of the mean-timer technique [21], which also returns the unknown bunch crossing originating the segment. In $r-z$ superlayers, only segments pointing to the interaction point are selected. The segments reconstructed in the two $r-\phi$ superlayers in each chamber are matched by the Track Correlator (TRACO), that improves the angular resolution thanks to the bigger lever arm. The Trigger Server (TS) selects, among all segment pairs in a chamber, the two corresponding to the highest p_T, and forwards them to the Drift Tube Track Finder (DTTF).

The DTTF matches the segments reconstructed in the four stations into a single muon track candidate, assigning the track parameters p_T, η, ϕ and a

quality word. This device is based on precomputed, memory-resident Look-Up Tables (LUT), which are used to extrapolate the segments between stations and to group matching segments. The track parameters are estimated with other LUTs on the basis of the the ϕ direction of the segments in the two innermost stations.

Finally, the candidates are sorted, and the four highest p_T muon candidates are delivered to the Global Muon Trigger.

The CSC Trigger. As for the barrel, the first trigger step in the endcaps is the local reconstruction. The CSC Local Trigger reconstructs segments independently using the strips and the wires of the six layers of each chamber. Cathode strips are used to reconstruct the ϕ coordinate and measure the transverse momentum of the track. First, the strips are digitised with half strip resolution, using a simple interpolation based on a comparator that analyses the charge in three adjacent strips. The hits in the six layers are then searched for patterns compatible with high-p_T tracks.

Anode wires are used to reconstruct the η coordinate and to provide a precise bunch crossing assignment. Wires are read out in groups of 5 to 16, to reduce the number of channels. Hit patterns compatible with a track coming from the nominal interaction point are searched for with a coincidence technique. A coincidence of two hits in different layers is needed to assign the bunch crossing, while the reconstruction of a segment requires four hits out of the six CSC planes.

Finally, the time coincidence of anode and cathode segments is required to construct three-dimensional segments. They are sent to the CSC Track Finder, which links the segments of the various stations to form a muon candidate and assigns p_T, η, ϕ and a quality word, using LUTs as in the case of the DTs.

The CSC system covers the region up to $|\eta| = 2.4$. However, the trigger electronics will not be installed in the region above $|\eta| = 2.1$ in the chamber ME1/1, effectively limiting the muon trigger geometrical acceptance to $|\eta| < 2.1$.

The RPC Trigger. No local reconstruction step is present in the RPC trigger [22], since the measurements in each chamber are simple points. The hits are collected by the Pattern Comparator Trigger (PACT), which looks for hits correlated in space and time in the four RPC stations. Hits are matched with pre-defined patterns in a large look-up table to provide identification and estimate of the p_T. The patterns allow to identify muons with at least three hits on four stations. In the case of the barrel, where six stations are present, the search is done independently for low-p_T muons in the first four layers (in MB1 and MB2) and for high-p_T ones using one layer in each station.

A ghost suppression algorithm is applied to reduce the effect of accidental

coincidences due to background hits. The four highest p_T candidates in the barrel and endcaps are then separately sent to the Global Muon Trigger.

The Global Muon Trigger. The task of the Global Muon Trigger (GMT) is to match the muon candidates from the different subsystems and combine their parameters in an optimal way. The matching is done by comparing the spatial coordinates of the segment (ϕ, η), and can be tuned to achieve the optimal balance between efficiency and background suppression. High efficiency can be obtained accepting candidates even if they are found by only one subsystem. Maximum background rejection can be obtained requiring all candidates to be reconstructed by both subsystems. The price is a lower efficiency. More refined criteria can be used; in the current implementation, candidates are accepted if they are reconstructed by two systems, otherwise they are selected on the basis of their quality word. Low-quality candidates from problematic η regions are discarded [23]. If two candidates are matched, the parameters of the track are chosen according to a programmable logic.

The GMT also assigns each candidate the MIP and Quiet bit of the corresponding calorimeter region (cf. Section 2.5.1.1). These bits can optionally be used to confirm the muon candidate and require that it is isolated. The performance of this selection is discussed in Section 5.1.

2.5.1.3 Performance of the Level-1 Muon Trigger Selection

The simplest possible Level-1 muon trigger selection is based on a threshold on the p_T of GMT tracks. The Level-1 p_T scale is defined at 90% efficiency, that is the scale where, for each given threshold, the efficiency for muons with a p_T equal to the threshold is 90% of the plateau efficiency. In other words, the p_T value reported by the trigger is such that there is only a 10% probability for the true value to be actually higher.

The resolution of the reciprocal of the transverse momentum, $1/p_T$, is shown in Fig. 2.16. The distributions are shifted with respect to zero due to the 90% scale definition. The resolution is about 17% in the barrel, 20% in the endcaps and 22% in the overlap region. Non-gaussian tails are present and, together with the limited resolution, are responsible for the "feed-through" of low p_T muons that are reconstructed at high momenta, thus passing typical trigger thresholds. This effect is important since the muon rate increases steeply for low p_T values, so that the contribution of feed-through muons to the Level-1 trigger rate is dominant even for high thresholds. This effect is visible in Fig. 2.17, where the spectrum of the generated p_T of muons passing a threshold of 14 GeV/c at low luminosity, and of 25 GeV/c at high luminosity, is shown.

This feed-through effect can be reduced only by improving the p_T resolution. This is the task of the Muon High Level triggers. The event rate corresponding

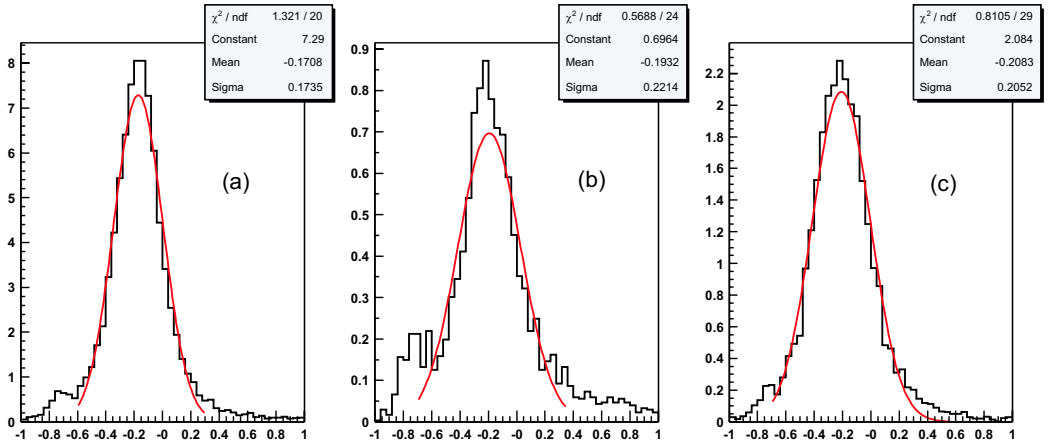

Figure 2.16: *Level-1 resolution on $1/p_T$ obtained with a sample of W decays at high luminosity for (a) the barrel region ($|\eta|$ <0.8); (b) the overlap region (0.8< $|\eta|$ <1.2); (c) the endcap region (1.2< $|\eta|$ <2.1) [1].*

to the selection of one or two muons at each trigger level (single- and di-muon selection) will be discussed in Section 4.7.

2.5.1.4 The Level-1 Trigger Table

The Level-1 trigger allows to define complex trigger algorithms based on the presence of several, different objects and on topological conditions and correlations. However, whenever possible, "inclusive" criteria should be used, to avoid biasing the sample of selected events. The simplest triggers are in general those based on the presence of one object with an E_T or p_T above a predefined threshold (single-object triggers) and those based on the presence of two objects of the same type (di-object triggers) with either symmetric or asymmetric thresholds. Other requirements are those for multiple objects of the same or different types ("mixed" and multiple-object triggers). In the case of special channels that are not efficiently selected by these simple criteria, very specific exclusive algorithms can be used. These cases are not discussed in the following.

The allocation of the Level-1 bandwidth to the different trigger streams is discussed in [1]. The choice of the Level-1 trigger thresholds is determined by the maximum event rate (bandwidth) that can be accepted by the DAQ system. The current estimate is that at startup the DAQ system will be able to handle an event rate of up to 50 kHz, which will be increased to 100 kHz when the full LHC design luminosity is reached. Only one third of this bandwidth is allocated, the rest being used as safety margin accounting for all uncertainties

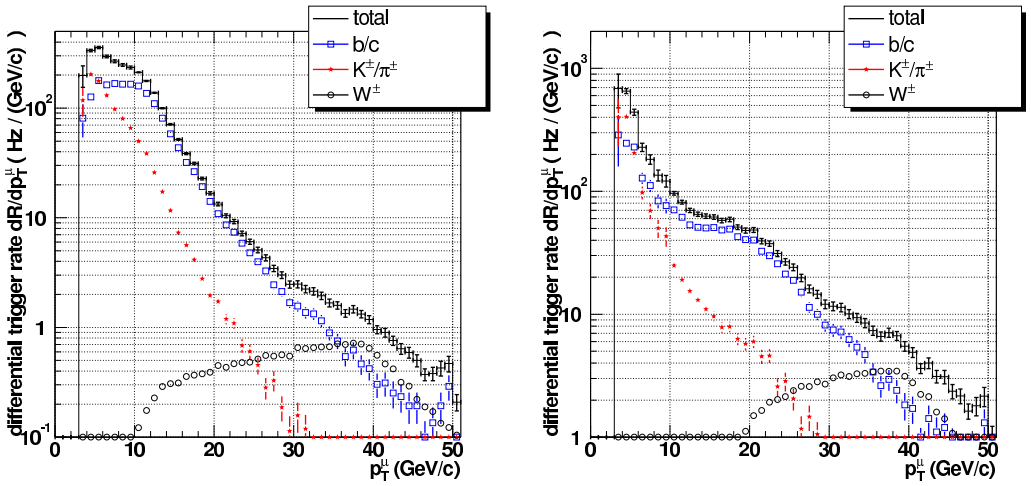

Figure 2.17: *Event rates as a function of the generated p_T for a Level-1 threshold of 14 GeV/c^2 at low luminosity (left) and of 25 GeV/c^2 at high luminosity (right). The separate contributions of b/c, K/π and W decays are shown [23].*

in the simulation of the basic physics processes, the CMS detector, and the beam conditions [1]. This bandwidth is then subdivided among the Level-1 objects described in the previous sections (muons, electrons and photons, tau jets, jets and combined channels) and for each of them between the single- and multiple-object streams.

The result is a set of thresholds called trigger table. The present Level-1 trigger tables at low and high luminosity are shown in Table 2.1 and Table 2.2, respectively.

Table 2.1: *L1 trigger table at low luminosity [1].*

Trigger	Threshold (GeV or GeV/c)	Rate (kHz)	Cumulative Rate (kHz)
Inclusive isolated electron/photon	29	3.3	3.3
Di-electrons/di-photons	17	1.3	4.3
Inclusive muon	14	2.7	7.0
Di-muons	3	0.9	7.9
Single tau-jet trigger	86	2.2	10.1
Two tau-jets	59	1.0	10.9
1-jet, 3-jets, 4-jets	177, 86, 70	3.0	12.5
Jet * ET miss	88 * 46	2.3	14.3
Electron * Jet	21 * 45	0.8	15.1
Minimum-bias (calibration)		0.9	16.0
Total			16.0

Table 2.2: *L1 trigger table at high luminosity [1].*

Trigger	Threshold (GeV or GeV/c)	Rate (kHz)	Cumulative Rate (kHz)
Inclusive isolated electron/photon	34	6.5	6.5
Di-electrons/di-photons	19	3.3	9.4
Inclusive muon	20	6.2	15.6
Di-muons	5	1.7	17.3
Single tau-jet trigger	101	5.3	22.6
Two tau-jets	67	3.6	25.0
1-jet, 3-jets, 4-jets	250, 110, 95	3.0	26.7
Jet * ET miss	113 * 70	4.5	30.4
Electron * Jet	25 * 52	1.3	31.7
Muon * Jet	15 * 40	0.8	32.5
Minimum-bias (calibration)		1.0	33.5
Total			33.5